AD-A021 249

CORRELATION OF BOW SHOCK PLASMA WAVE TURBULENCE WITH SOLAR WIND PARAMETERS

Paul Rodriguez, et al

Iowa University

Prepared for:

Office of Naval Research

April 1975

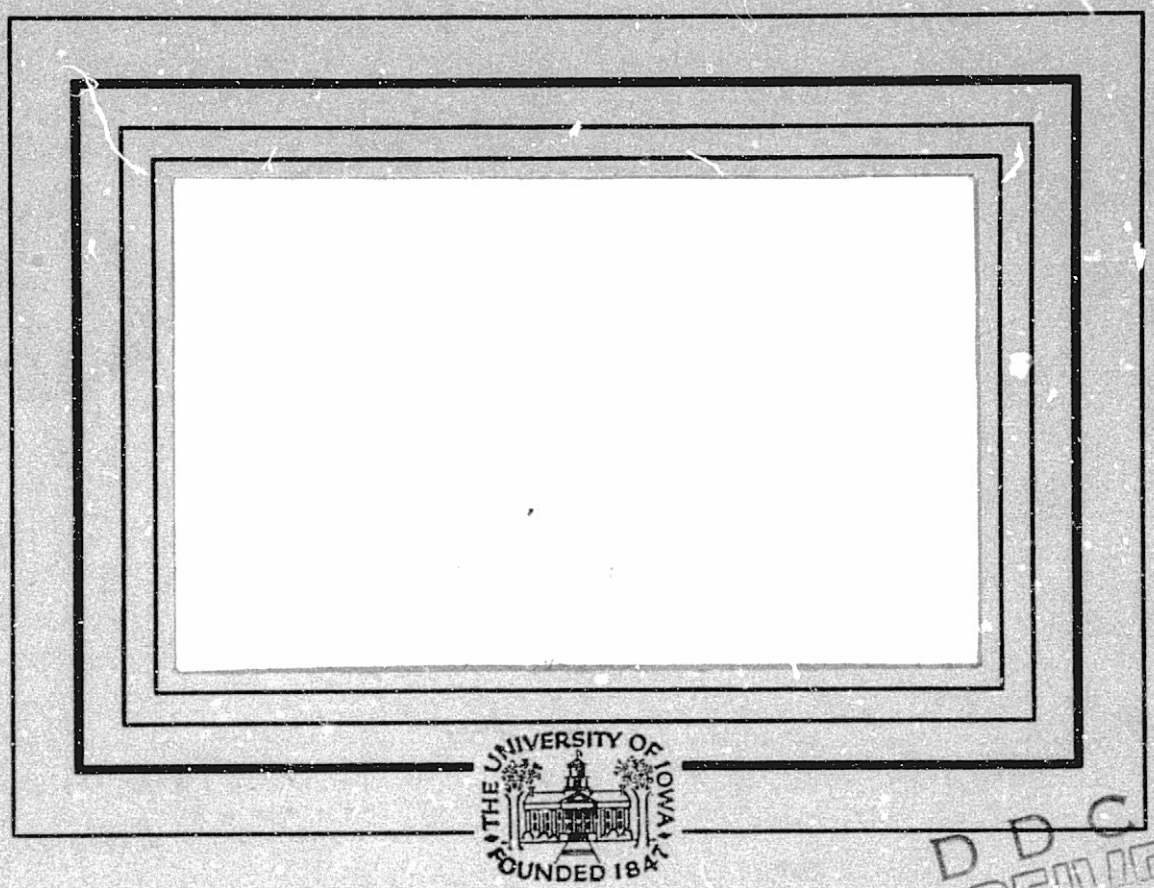

Research was supported in part by the Office of Naval Research
under Contract N00014-68-A-0196-0009.

Department of Physics and Astronomy

THE UNIVERSITY OF IOWA

Iowa City, Iowa 52242

Correlation of Bow Shock Plasma Wave Turbulence with Solar Wind Parameters

by

Paul Rodriguez
and
Donald A. Gurnett

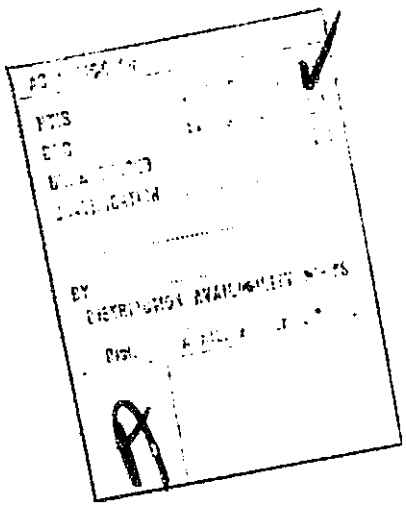

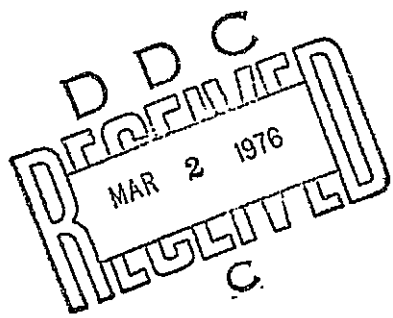

April, 1975

The Department of Physics and Astronomy
The University of Iowa
Iowa City, Iowa 52242

This work was supported in part by the National Aeronautics and Space Administration under Contract NAS5-11074 and Grants NGL-16-001-002 and NGL-16-001-043 and by the Office of Naval Research under Grant N00014-68-A-0196-0009.

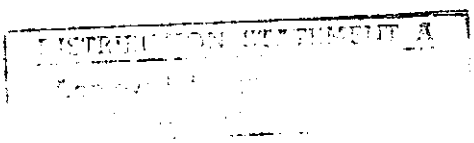

UNCLASSIFIED

SECURITY CLASSIFICATION OF THIS PAGE (When Data Entered)

1.

REPORT DOCUMENTATION PAGE		READ INSTRUCTIONS BEFORE COMPLETING FORM
1. REPORT NUMBER: U. of Iowa 75-18	2. GOVT ACCESSION NO.	3. RECIPIENT'S CATALOG NUMBER
4. TITLE (and Subtitle): CORRELATION OF BOW SHOCK PLASMA WAVE TURBULENCE WITH SOLAR WIND PARAMETERS		5. TYPE OF REPORT & PERIOD COVERED: Progress, April, 1975
		6. PERFORMING ORG. REPORT NUMBER
7. AUTHOR(s): Paul Rodriguez and Donald A. Gurnett		8. CONTRACT OR GRANT NUMBER(s): N00014-68-A-0196-0009
9. PERFORMING ORGANIZATION NAME AND ADDRESS: Department of Physics and Astronomy, The University of Iowa, Iowa City, Iowa 52242		10. PROGRAM ELEMENT, PROJECT, TASK AREA & WORK UNIT NUMBERS
11. CONTROLLING OFFICE NAME AND ADDRESS: Office of Naval Research, Arlington, Virginia 22217		12. REPORT DATE: April 1975
		13. NUMBER OF PAGES: 65
14. MONITORING AGENCY NAME & ADDRESS (if different from Controlling Office)		15. SECURITY CLASS. (of this report): UNCLASSIFIED
		15a. DECLASSIFICATION/DOWNGRADING SCHEDULE

16. DISTRIBUTION STATEMENT (of this Report)

Approved for public release; distribution is unlimited.

17. DISTRIBUTION STATEMENT (of the abstract entered in Block 20, if different from Report)

18. SUPPLEMENTARY NOTES

To be published in J. Geophys. Res.

19. KEY WORDS (Continue on reverse side if necessary and identify by block number)

Bow Shock
Plasma Wave Turbulence
Structure of the Shock

20. ABSTRACT (Continue on reverse side if necessary and identify by block number)

[See page following]

DD FORM 1 JAN 73 1473 EDITION OF 1 NOV 65 IS OBSOLETE
S/N 0102-014-6601

UNCLASSIFIED

SECURITY CLASSIFICATION OF THIS PAGE (When Data Entered)

ABSTRACT

The r.m.s. field strengths of electrostatic and electromagnetic turbulence in the earth's bow shock, measured in the frequency range 20 Hz to 200 kHz with IMP-6 satellite, are found to correlate with specific solar wind parameters measured upstream of the bow shock. The largest r.m.s. field strengths of electrostatic turbulence (200 Hz - 4 kHz) occur when the upstream electron to proton temperature ratio T_e/T_p is large, and when the proton temperature T_p is small, indicating that the mechanism for generating electrostatic turbulence in the bow shock is more efficient when lower upstream proton temperatures occur. No substantial correlation is found between the r.m.s. field strengths of electrostatic turbulence and three upstream parameters commonly used to classify the magnetohydrodynamic structure of the turbulent bow shock: the Alfven Mach number M_A, the ratio of particle pressure to magnetic field pressure β, and the shock normal angle $\psi(\vec{B},\hat{n})$. The strong correlation with T_e/T_p and T_p, and the lack of strong correlation with M_A, β, and $\psi(\vec{B},\hat{n})$ indicates that the strength of electrostatic turbulence in the bow shock is determined by the kinetic properties of the solar wind plasma rather than by its fluid properties.

The largest r.m.s. field strengths for electromagnetic turbulence (20 Hz - 4 kHz) occur when the upstream particle density N

is large and when the shock normal angle $\psi(\vec{B},\hat{n})$ is closer to 90°, supporting a previous conclusion that whistler waves comprise the electromagnetic turbulence in the bow shock. Electric field turbulence, composed of both electrostatic and electromagnetic fluctuations, correlates with the upstream parameters T_e/T_p, T_p, and $\psi(\vec{B},\hat{n})$ in such a way as to imply that mode coupling occurs between electrostatic and electromagnetic waves.

A broad spectrum of high frequency (3 - 30 kHz) electrostatic turbulence typically observed in the leading edge of the bow shock is interpreted as indicating the region of electron heating. Deeper within the shock transition the intensity of low frequency (< 3 kHz) electrostatic turbulence greatly increases to form a broad peak, centered between 200 - 800 Hz, and is interpreted as corresponding to the region of maximum proton heating. The characteristic development of the electric field spectrum through the shock transition indicates that strong coupling exists between the electron and proton heating processes.

I. INTRODUCTION

Several studies of the earth's bow shock have shown that a complex structure of wave-particle interactions govern the heating of solar wind electrons and ions as they stream across the shock transition. Fredricks et al. [1968, 1970a, b] have shown that electrostatic turbulence at 1.3 kHz and the scattering of protons correlates with the gradients in the magnetic field at the shock front, thus indicating the presence of a current-driven instability. Montgomery et al. [1970] and Formisano and Hedgecock [1973a, b] have shown that electron thermalization occurs in a thin region upstream of the bow shock, followed by ion thermalization in the main shock transition. Solar wind ions are reported by Neugebauer [1970] to be substantially decelerated near the upstream side of the bow shock, possibly by a charge separation electric field. Neugebauer et al. [1971] have reported the observation of ELF magnetic field oscillations (10 - 1000 Hz) correlated with superthermal electrons ($>$ 100 ev) in the shock magnetic field gradient. Holzer et al. [1966, 1972] and Olson et al. [1969] have discussed the spectrum of magnetic field fluctuations in the bow shock below about 100 Hz which shows a broad noise spectrum with a peak near 3 Hz, and includes waves that propagate in the shock frame both upstream and downstream. Fairfield [1974] has studied whistler waves in the frequency range 0.5 - 4.0 Hz which are detected

ahead of the bow shock and may result from resonant interactions with upstream electrons. The spectrum of plasma wave turbulence in the bow shock, as measured with the University of Iowa plasma wave spectrum analyzers on the IMP-6 satellite, was reported in Rodriguez and Gurnett [1975]. Whistler waves and electrostatic waves are shown by Rodriguez and Gurnett to be the major components of the bow shock spectrum between 20 Hz and 200 kHz.

In our previous report [Rodriguez and Gurnett, 1975], hereafter referred to as paper I, it was shown that the characteristic electric field spectrum of the bow shock can be resolved into a low frequency electromagnetic component (20 Hz - 200 Hz) which decreases monotonically with increasing frequency approximately as $f^{-(2.0 \pm 0.5)}$ and a higher frequency electrostatic component (200 Hz - 4 kHz) associated with a peak in the electric field spectrum between about 200 Hz to 800 Hz. The characteristic magnetic field spectrum of the bow shock was shown to decrease monotonically with frequency approximately as $f^{-(4.0 \pm 0.5)}$ and to display an upper cutoff frequency near the electron gyrofrequency. By taking the ratio ϵ_E/ϵ_B of simultaneously measured electric and magnetic field energy densities in the bow shock, it was shown in paper I that ϵ_E/ϵ_B increased nearly monotonically from values near 10^{-4} - 10^{-3} at 20 Hz to 10^{+2} - 10^{+3} at 1 kHz. The values of ϵ_E/ϵ_B (proportional to n^{-2} where n is the index of refraction) at low frequencies and the observed upper cutoff frequency near the electron gyrofrequency in the shock magnetic field spectrum led to the conclusion in paper I that in the range 20 Hz - 200 Hz the electric and magnetic field turbulence in the shock is caused by electromagnetic whistler waves.

It was also concluded that the large values of $\varepsilon_E/\varepsilon_B$ at frequencies greater than about 200 Hz showed that these higher frequency waves are almost completely electrostatic and are associated with the peak centered between 200 - 800 Hz in the shock electric field spectrum.

The frequency range (20 Hz - 200 kHz) of the shock plasma wave spectra discussed in paper I includes all the characteristic plasma frequencies for electrons and protons except for the proton gyrofrequency (~ 0.1 Hz). The heating of solar wind electrons and protons in the bow shock must result in the self-consistent generation of a spectrum of turbulent electric fields. It is expected that such a spectrum will be broad enough to include most of the characteristic plasma frequencies since these are the elementary excitations through which the particle velocity distributions can be broadened. Therefore, it is assumed that the electric field spectra of paper I and of this study are closely related to the dissipative processes that occur in the bow shock.

II. INTENSITY VARIABILITY OF SHOCK TURBULENCE

A. Dynamic Range

The variability of plasma wave turbulence in the bow shock is indicated in Figures 1 and 2 (similar to Figures 7 and 8 of paper I). In Figure 1, two kinds of electric field spectra are shown, spectra measured with a 5.12 seconds averaging time (averages) and spectra measured with a 0.1 second averaging time (peaks). One measurement of the peak spectrum is obtained within the time period of one measurement of the average spectrum. (A description of the University of Iowa plasma wave experiment and the spectrum analyzer used to measure the electric and magnetic field spectra in the bow shock is given in paper I.) The left hand side of Figure 1 is an overlay of average electric field spectra that were measured in 36 crossings of the bow shock; the right hand side is an overlay of the corresponding peak electric field spectra. Figure 1 thus illustrates the dynamic range of intensities that have been sampled for electric field turbulence in the bow shock. For example, on different shock crossings the average electric field spectral densities at 1 kHz ranges from a minimum of 3×10^{-13} volts^2 m^{-2} Hz^{-1} to a maximum of 6×10^{-9} volts^2 m^{-2} Hz^{-1}, a dynamic range of over four orders of magnitude. A similar range of variation is seen in the peak spectral densities. For each spectrum of Figure 1, a total r.m.s. field strength E_{rms} may be computed by

integrating the spectrum from 20 Hz to 200 kHz. The range of E_{rms} so obtained is $(4.0 - 0.19) \times 10^{-3}$ volts m^{-1} for the average spectra and $(23. - 2.1) \times 10^{-3}$ volts m^{-1} for the peak spectra. The electrostatic and electromagnetic components of the shock spectrum which were described above are evident in the characteristic shape of the spectra of Figure 1, with the best resolution of the two components occurring in the average spectra of intermediate intensity. For average spectra of greatest intensity it can be seen that the peak centered between 200 Hz and 800 Hz broadens out enough to nearly fill in the minimum in the curve at about 200 Hz where the two components of the spectrum meet. For the average spectra of smallest intensity, the peak nearly disappears.

Figure 2 shows the average and peak magnetic field spectra corresponding to, and in the same format as, the average and peak electric field spectra of Figure 1. There is evidently a smaller dynamic range for the magnetic field spectral densities (about two orders of magnitude at 100 Hz), and except for a few peak spectra, the shape of the spectrum has the characteristic monotonic decrease with frequency associated with the component below about 200 Hz in the electric field spectrum. The plasma wave turbulence associated with the broad peak in the average spectra of Figure 1 is clearly electrostatic turbulence since there is no corresponding peak in the magnetic field spectra of Figure 2.

B. Correlation Parameters

Since plasma shock waves are usually categorized in terms of such upstream parameters as the Alfven Mach number M_A, the ratio of

particle pressure to magnetic field pressure β, the ratio of electron to proton temperatures T_e/T_p, and the shock normal angle $\psi(\vec{B},\hat{n})$, it is of interest to investigate the relationship between these parameters and the intensity variability of bow shock turbulence indicated by Figures 1 and 2. The upstream parameters used in this study are derived from the measurements of two other IMP-6 experiments, the Los Alamos Scientific Laboratory plasma analyzer, which provides a measurement of the velocity distribution of solar wind particles with a minimum time resolution of about 90 seconds, and the Goddard Space Flight Center (GSFC) magnetometer, which measures the magnetic field magnitude and direction with a time resolution of 80 milliseconds. In addition to M_A, β, T_e/T_p, and $\psi(\vec{B},\hat{n})$ other upstream parameters used are the upstream magnetic field magnitude $|\vec{B}|$, the magnetosonic Mach number M_s, solar wind velocity V_{sw}, Alfven speed C_A, the sound speed C_s, and the particle density N. The r.m.s. field strengths for the electromagnetic and electrostatic components in 5.12 - seconds average shock spectra like those in Figures 1 and 2 are used as the measure of the intensity of shock turbulence. We define $E_{rms,1}$ and $E_{rms,2}$ as the r.m.s. electric field strengths obtained from the average shock electric field spectrum by integrating from 20 Hz to 200 Hz, and from 200 Hz to 4 kHz, respectively. $E_{rms,1}$ and $E_{rms,2}$ are thus the r.m.s. electric field strengths of the electromagnetic and electrostatic components, respectively, of the shock electric field spectrum. B_{rms} is the r.m.s. magnetic field strength of the electromagnetic component, obtained by integrating the average shock magnetic field spectrum from 20 Hz to 4 kHz. The approach

of this study is to seek correlation between the values of $E_{rms,1}$, $E_{rms,2}$, and B_{rms}, and the values of M_A, M_s, β, T_e/T_p, V_{sw}, C_A, C_s, N, T_e, T_p, $\psi(\vec{B},\hat{n})$, and $|\vec{B}|$.

Simultaneous measurement of the spectrum of bow shock turbulence and upstream solar wind parameters is not possible with a single satellite, so the solar wind parameters derived from the plasma analyzer measurements are averages over time periods during which IMP-6 was in the upstream region near the bow shock. The solar wind parameters are averaged over one to two hour periods, before or after the shock crossing at which the corresponding plasma wave spectrum is measured, to obtain values which characterize the solar wind properties near the time of the shock crossing. The one to two hour averaging periods also makes the solar wind parameters relatively independent of short period fluctuations. If multiple shock crossings take place in a time interval less than the averaging times of solar wind parameters, the corresponding series of r.m.s. field strengths for shock turbulence is averaged over the number of crossings. The values of shock normal angles $\psi(\vec{B},\hat{n})$ are computed from the model of Fairfield [1971] using 4-seconds averages of the GSFC magnetometer measurements near the leading edge of each shock crossing.

The distributions of values for the upstream parameters used in this study are shown in the histograms of Figures 3 and 4. The general shapes of the distributions compare favorably with the corresponding distributions which are obtained for the solar wind when

many more samples are taken [Formisano and Moreno, 1974]. The solar wind parameters of the present study thus approximate the typical ranges of solar wind conditions. The minimums, maximums, means, and standard deviations for the distributions of Figures 3 and 4 are listed in Table 1.

Energy densities for the electromagnetic and electrostatic components of the bow shock spectrum may be computed from $\epsilon(E_{rms,i}) = E^2_{rms,i}/8\pi$ (i = 1, 2) and $\epsilon(B_{rms}) = B^2_{rms}/8\pi$, where Gaussian units are used for the electric and magnetic fields. The relationship of $\epsilon(E_{rms,i})$ and $\epsilon(B_{rms})$ to the solar wind energy density

$$\epsilon(SW) = \frac{1}{2} Nm_p V^2_{SW} + \frac{5}{2} NK_B(T_e + T_p) \quad ,$$

where m_p is the proton mass and K_B is Boltzmann's constant, is indicated by the distributions of the ratios $\epsilon(E_{rms,i})/\epsilon(SW)$ and $\epsilon(B_{rms})/\epsilon(SW)$ shown in Figure 5. It is evident that the plasma wave energy densities in the bow shock are always very small fractions of the solar wind energy density. The absolute energy density distributions for the bow shock electromagnetic and electrostatic components, and for the solar wind are shown in Figure 6. Table 2 list the characteristic parameters for the distributions of Figures 5 and 6.

C. Linear Correlation Coefficients

A standard statistical correlation technique (least squares fitting) has been used to calculate linear correlation coefficients that indicate the degree of association between the r.m.s. field

strength of shock turbulence and solar wind parameters. The fitting equation used is log y = bx + a, where y is the r.m.s. field strength, x is the plasma parameter, and b and a are constants. The choice of fitting equation is not based on any theoretical relationship between the parameters, but is used only to provide a quantitative measure (the correlation coefficient) with which to judge the statistical dependence (or independence) of the parameters involved. Since the measurements of electric and magnetic field amplitudes are obtained from antenna voltages which are digitized with equal quantizing steps on a logrithmic scale, the relative uncertainty $\Delta V/V$ in the measured signal voltages is constant. Therefore, the least squares fitting is done with constant relative uncertainty in the r.m.s. field amplitudes [Bevington, 1969, p. 180].

Table 3 lists the linear correlation coefficients R obtained for the two-parameter fits. For S points used in the least squares fit, R_c is the critical value of the correlation coefficient at the 1% level of significance for a two-parameter fit [Neville and Kennedy, 1964, p. 314]. If the absolute value of the computed correlation coefficient $|R|$ exceeds R_c, the probability is 1% that the observed correlation between the two parameters is due to chance alone. Therefore, a strong correlation is indicated by a large value of R compared to R_c.

III. ELECTROSTATIC TURBULENCE

A study of the coefficients in Table 3 reveals that the electrostatic field strength $E_{rms,2}$ is strongly correlated with several of the solar wind parameters. In particular, $E_{rms,2}$ and T_e/T_p have the largest value of R, indicating that a strong positive correlation exists between the intensity of electrostatic turbulence in the bow shock and the electron to proton temperature ratio in the upstream solar wind. Figure 7 shows the plot of $E_{rms,2}$ against T_e/T_p. The diagonal dashed line in Figure 7 is the line of regression for $E_{rms,2}$ on T_e/T_p, and the slope of this line indicates the apparent dependence of $E_{rms,2}$ on T_e/T_p. The large error bars are at $\pm \sigma(y)$, the standard deviation, above and below the line of regression and indicate the degree of dispersion of the data points about the mean. However, in this case the large dispersion does not mean that large measurement errors are present in the values of $E_{rms,2}$. The dispersion of the values of $E_{rms,2}$ is probably indicative of the dependence of $E_{rms,2}$ on other parameters besides T_e/T_p which are not included in the two-parameter fit. As is shown in Table 3, $E_{rms,2}$ displays significant correlation ($R > R_c$) with other shock parameters, so that the total dependence of $E_{rms,2}$ is very likely a complex function of T_e/T_p, T_p, C_s, etc. Also, the one to two hours averaging period for the solar wind

parameters removes short period fluctuations from these upstream values which may be related to some of the scatter in $E_{rms,2}$. In addition, the electric field measurements are made with a single antenna so that only one component of the electric field is detected at any instant. However, as shown in paper I, the electric field turbulence in the bow shock has a broad angular distribution, and a measurement averaged over 5.12 seconds (~ half the spin period) can be assumed to be close to the total field magnitude. Considering then the approximations involved in a two-parameter fit, it can be expected that a true, but weak, dependence of $E_{rms,2}$ on an upstream parameter may not emerge from the correlations in this study. However, a strong, and therefore more important, dependence of $E_{rms,2}$ on an upstream parameter should be evident in the correlations, even though the functional relationship between $E_{rms,2}$ and the upstream parameter is not known. The slope of the regression line is the important measure of association between $E_{rms,2}$ and T_e/T_p, and since the regression line is a mean fit, the standard deviation of the mean, $\sigma(\bar{y})$, is a better measure of dispersion because this tends to compensate for correlations not included in a two-parameter fit. The smaller error bars in Figure 7 are at the 1% level of significance, $\pm 2.576\ \sigma(\bar{y})$. At their location on the regression line, the small error bars also indicate the 1% limits to the dispersion of the slope when the regression line is rotated about its centroid. It is clear that the slope of the regression line changes neither in sign nor greatly in magnitude at these two limits.

The second strongest correlation of $E_{rms,2}$ is with the proton temperature T_p. The plot of $E_{rms,2}$ against T_p is shown in Figure 8, where the line of regression for the two-parameter fit is the diagonal dashed line and the error bars have the same meaning as in Figure 7. The slope of the regression line indicates that a negative correlation exists between electrostatic turbulence in the bow shock and the upstream proton temperature. Since no significant correlation is found between $E_{rms,2}$ and the electron temperature T_e, it appears that in the relationship between $E_{rms,2}$ and the ratio T_e/T_p of Figure 7, variations in the upstream proton temperature T_p is the significant factor. Therefore we conclude that the instability mechanism that produces electrostatic turbulence in the bow shock is primarily associated with the value of T_e/T_p, and that the proton temperature T_p serves to modulate the efficiency of that mechanism. Table 3 also shows that $E_{rms,2}$ has a significant negative correlation with the sound speed C_s, which is already implicit in the correlations with T_e/T_p and T_p if we note that $C_s \propto [T_e + T_p]^{1/2} = [T_p(T_e/T_p + 1)]^{1/2}$. It may also be observed that $E_{rms,2}$ shows a negative correlation with V_{sw}, only marginal correlations with other parameters such as M_A and perhaps β, and no correlation with $\psi(\vec{B},\hat{n})$.

In the column under $E_{rms,1}$, the r.m.s. electric field strength between 20 Hz and 200 Hz, it can be seen that $E_{rms,1}$ has its strongest correlation with T_e/T_p; the corresponding points are plotted in Figure 9. A comparison of the correlation coefficients in Table 3 reveals that $E_{rms,1}$ and $E_{rms,2}$ have like correlations with T_e/T_p, T_p, and C_s,

i.e., with the same sign and ordering. However, $E_{rms,1}$ also correlates with $\psi(\vec{B},\hat{n})$, unlike $E_{rms,2}$, but instead like B_{rms}. The correlations of $E_{rms,1}$ with T_e/T_p, T_p, C_s, and $\psi(\vec{B},\hat{n})$ thus indicate that the dependence of $E_{rms,1}$ on the upstream parameters includes characteristics of both purely electrostatic turbulence and purely electromagnetic turbulence. We may therefore conclude that in the low frequency portion of the shock spectrum the electric field is derived from the fields of coupled electrostatic and electromagnetic waves. A similar conclusion was reached in paper I where it was shown that below about 200 Hz the ratio of electric field energy density to magnetic field energy density ϵ_E/ϵ_B is greater than expected for whistler waves, and that therefore the electric field energy density ϵ_E must also include electrostatic waves. It can thus be seen that the entire shock electric field spectrum is primarily composed of electrostatic waves, which couple to whistlers at frequencies below the electron gyrofrequency. An electrostatic wave which can couple to whistlers in a high β plasma such as the solar wind is the ion sound wave [Formisano and Kennel, 1969]. From the discussion of Formisano and Kennel [1969] it may be inferred that whistlers and ion sound waves can couple over a broad range of frequencies below the electron gyrofrequency whenever strong temperature gradients occur; this result is consistent with the observations of electrostatic and electromagnetic waves below about 200 Hz in the bow shock spectrum.

The observed correlations of $E_{rms,1}$ and $E_{rms,2}$ with T_e/T_p and T_p imply that the kinetic properties of the solar wind plasma, i.e., the wave-particle interactions that modify the electron and proton

velocity distributions, are the primary factors determining the intensity of electrostatic turbulence in the bow shock. Usually $T_e > T_p$ in the upstream region and leading edge of the shock. The observation of temperature jumps in T_e and T_p across the shock such that T_p is 2-4 times greater than T_e in the near downstream region means that protons provide the major dissipation mechanism for the bow shock [Montgomery et al., 1970]. The electric field spectrum from which $E_{rms,1}$ and $E_{rms,2}$ are computed can thus be associated with proton heating.

Such fluid parameters as M_A, β, and $\psi(\vec{B},\hat{n})$, with which $E_{rms,1}$ and $E_{rms,2}$ have weak or null correlations, are apparently not important determinants of the intensity variations in the shock electric field spectrum. However, it should be noted that the m.h.d. structure of the bow shock is often classified in terms of M_A, β, and $\psi(\vec{B},\hat{n})$ [Formisano and Hedgecock, 1973a; Greenstadt, 1974], and within these classifications, almost all of the shocks used in the correlations of Table 3 fall into the category in which the bow shock is most often found, that of "turbulent shocks" with $M_A > 3$, $\beta > 0.1$, and $\psi(\vec{B},\hat{n}) \sim 30° - 70°$. Certain critical values of the upstream fluid parameters, $M_A^* \sim 2.5 - 3.0$, $\beta \sim 0.1$, and $\psi(\vec{B},\hat{n}) = 88.7°$, at which significant changes in the m.h.d. structure of collisionless shocks occur [Woods, 1969a, b, 1970; Paul, 1972; Tidman and Krall, 1971, chap. 3; Biskamp, 1973] are not well represented in the correlations of Table 3.

IV. ELECTROMAGNETIC TURBULENCE

For the upstream parameters of Table 3, electromagnetic turbulence, represented by the magnetic field strength B_{rms}, is found to display a strong correlation with the particle density N. Figure 10 shows the plot of B_{rms} and N; the line of regression and error bars have the same meaning as in previous figures. The slope of the regression line indicates that more intense magnetic field fluctuations occur for larger values of the particle density, a variation consistent with whistler waves since the index of refraction (= cB/E) for the whistler mode increases with particle density. The positive correlation between B_{rms} and N supports the previous conclusion that whistler waves comprise the shock magnetic field spectrum. The slope of the regression line in Figure 10 is not drastically changed if the relatively few points at high density are omitted from the fit.

The shock normal angle $\psi(\vec{B},\hat{n})$ is the only other parameter of Table 3 with which B_{rms} shows a substantially significant correlation. The plot of B_{rms} and $\psi(\vec{B},\hat{n})$ is shown in Figure 11. $\psi(\vec{B},\hat{n})$ takes values in the range 0° to 90°, with $\psi(\vec{B},\hat{n}) = 0°$ being defined as a parallel shock, $0° < \psi(\vec{B},\hat{n}) \leq 88.7°$ is an oblique shock, and $88.7° < \psi(\vec{B},\hat{n}) \leq 90°$ is a perpendicular shock. These definitions for $\psi(\vec{B},\hat{n})$ are theoretical [Tidman and Krall, 1971, p. 24]; the experimental values for shock normal angles have error limits of $\pm$ (5° - 10°) so that

most shocks can be considered as oblique, $\psi(\vec{B},\hat{n}) \sim 0°$ to $85°$, or perpendicular, $\psi(\vec{B},\hat{n}) \sim 85°$ to $90°$. Other classifications are also used [Greenstadt, 1974]. Whistlers propagate in a cone about the direction of $\vec{B}$, therefore as $\vec{B}$ lies closer to the plane of the shock, i.e., as $\psi(\vec{B},\hat{n}) \to 90°$, then on the average it can be expected that the energy density of whistler waves in the plane of the shock will increase. Therefore, the positive correlation of B_{rms} and $\psi(\vec{B},\hat{n})$ also supports the identification of B_{rms} as whistler turbulence.

The frequency range of B_{rms} (20 Hz - 4 kHz) corresponds to the high frequency end of a much broader spectrum of magnetic field fluctuations of the bow shock region which generally has its largest spectral densities at frequencies near and below the proton gyrofrequency (0.001 - 1.0 Hz) [Holzer et al., 1966, 1972; Olson et al., 1969; Fairfield and Ness, 1970]. Since most of the magnetic field energy density is at the much lower frequencies associated with the m.h.d. regime, it is not surprising that B_{rms} has insignificant correlations with m.h.d. fluid parameters such as M_A and β.

A positive correlation between B_{rms} and the upstream magnetic field magnitude $|\vec{B}|$ is also indicated in Table 3. The observed correlation is not related to the shift of the whistler cutoff, i.e., the electron gyrofrequency, toward a higher frequency in the spectrum of magnetic field fluctuations since for a typical spectrum that varies as f^{-4} the largest expected upward shift in the whistler cutoff increases B_{rms} by only about 1%, whereas the values observed for B_{rms} range over

more than an order of magnitude. The correlation of B_{rms} with $|\vec{B}|$ thus indicates an actual statistical increase in the intensity of magnetic field fluctuations with an increase in $|\vec{B}|$. The correlation appears to be weak, however.

V. BOW SHOCK STRUCTURE

The leading edge of a collisionless plasma shock wave has been considered in theoretical studies to be a region where particle reflection and heating can occur which greatly influence the dissipation processes further into the shock [Woods, 1969b, 1971; Biskamp, 1970, 1973; Biskamp and Welter, 1972; Tidman and Krall, 1971, p. 130]. Experimental measurements of electron and ion velocity distributions near the earth's bow shock have shown that electron preheating and ion deceleration does occur near the foot of the magnetic field gradient [Montgomery et al., 1970; Neugebauer, 1970; Neugebauer et al., 1971]. The leading edge and transition region of the bow shock can often be resolved in the structure of the plasma wave spectra that are obtained at a given shock crossing. It may therefore be expected that electron preheating should result in a broad spectrum of turbulent electrostatic waves at the leading edge of the bow shock. In fact, electrostatic waves are typically observed on the upstream side of the transition region in almost all bow shock crossings that we have studied. In the main transition region of the shock the spectrum of plasma waves is modified significantly and can be associated with the ion thermalization that provides the major dissipation for the shock [Montgomery et al., 1970].

The data in Figure 12 were obtained for a perpendicular shock with the transition region clearly defined. The upper panel shows the electric field in the 3.11 kHz channel of the University of Iowa spectrum analyzer which was measured with the rapid-sample mode described in paper I. The magnetic field measured by the GSFC magnetometer is shown in the lower panel. The angles ϕ_B and θ_B are the solar ecliptic longitude and latitude of $\vec{B}$. Before about 1440:38 UT the spacecraft is in the quiet upstream solar wind. At 1440:38 UT the leading edge of the bow shock is encountered as shown by the sudden increase in electric field strength above the solar wind noise level and the corresponding onset of fluctuations in the magnetic field. It can be seen that the electric field increases substantially in the time interval between the vertical dashed lines (a) and (b), before the main gradient of the magnetic field which occurs in the time interval between vertical dashed lines (b) and (c). Since the spectrum of electron plasma oscillations (peaked at about $f_{pe} \sim$ 30 kHz) is often observed to broaden toward 3.11 kHz upstream of the bow shock, the electrostatic noise between points (a) and (b) in Figure 12 may indicate a heating of the solar wind electron distribution just before the main gradient of the magnetic field occurs. Such preheating of electrons would substantially increase the value of T_e/T_p in the leading edge of the shock with a consequent lowering of the threshold for the destabilization of drift currents such as occur with ion sound waves [Tidman and Krall, 1971, p. 128]. The electrostatic turbulence between (b) and (c) correlates well with the

magnetic field gradient, similar to the results of Fredricks et al. [1968, 1970b]. It can be expected that most of the ion thermalization must occur in the region of this large gradient [Montgomery et al., 1970; Greenstadt et al., 1975]. It is clear that in the shock crossing of Figure 12, the structure of electrostatic turbulence in the leading edge of the shock is not greatly different from that in the main transition indicating that the regions of electron and ion heating overlap. In the immediate downstream region, the electric field noise intensity at 3.11 kHz shows a series of nearly periodic fluctuations that display exponentially decreasing magnitude. The periodicity of the larger downstream fluctuations is not related to the spacecraft spin period, so it may be assumed that the fluctuations are real time variations of electrostatic turbulence. The exponential envelope of the downstream fluctuations implies that the spectrum of electrostatic waves is being damped, perhaps by the type of fluctuations in the ion distribution observed by Montgomery et al. [1970] in the downstream region.

A second example of a perpendicular shock in which the structure of the transition region is clearly defined is shown in Figure 13. The upper panel shows the electric field in four channels (36 Hz, 311 Hz, 3.11 kHz, 31.1 kHz) of the plasma wave spectrum analyzer, with average measurements plotted as vertical bars and peak measurements indicated by dots. The magnitude and direction angles of the magnetic field measured simultaneously by the GSFC magnetometer is shown in the lower panel. A vertical dashed line at about 2219:00 UT

marks the time at which the shock transition region begins as determined by the electric field measurements. It can be seen that the electric field noise begins almost one minute before the main gradient of the magnetic field. The shock transition region is fairly wide in time and the 5.12-seconds average measurements can resolve the changes in the electric field spectrum as the transition region is traversed. The beginning of the transition region is detected simultaneously in all channels; however, the rise times to maximum electric field intensity in the transition region is progressively shorter for increasing frequency. The relaxation from maximum intensity in the two high frequency channels begins before the maximum intensity is reached in the two low frequency channels so that by the time the maximum field strength occurs at 311 Hz, the electric field intensity at 31.1 kHz is nearly back to the noise level. The magnetic field measurements indicate that the electrostatic turbulence at lower frequencies correlates with the main transition region while the electrostatic turbulence at high frequencies correlates with the leading edge of the bow shock.

Between 2219:20 and 2220:00 UT, when the spacecraft was in the leading edge of the shock transition, a rapid-sample measurement of the 31.1 kHz electric field channel occurred. The rapid-sample data is shown in the polar plot of Figure 14 in which the electric field measurements are plotted versus the spin angle of the spacecraft antenna in the solar ecliptic plane. During the time of the rapid-

sample measurements the average magnetic field direction in the leading edge of the bow shock had a solar ecliptic latitude $\theta_B \sim 30°$ and a solar ecliptic longitude $\phi_B \sim 90°$. The projection of the magnetic field vector into the solar ecliptic plane at $\phi_B \sim 90°$ is indicated in the polar plot of Figure 14. By computing the second moments of the rapid-sample measurements about the solar ecliptic x and y axes (equivalent to evaluating the moments of inertia for unit "mass" particles with moment arms equal to the fluctuation amplitudes) and diagonalizing the resulting matrix, the principal axes may be obtained for the two-dimensional distribution of rapid-sample measurements. The direction of the major principal axis, indicated by φ_p on the polar plot, represents the average polarization direction of the electric field fluctuations. It is evident that the average electric field polarization is nearly aligned with the magnetic field vector direction ($\phi_B - \phi_p \sim 10°$); the frequency and average polarization therefore identify the noise as electron plasma oscillations [Fredricks et al., 1968, 1970b; Rodriguez and Gurnett, 1975]. The spectrum of electron plasma oscillations at about 2219:00 UT (20 seconds before the rapid-sample data of Figure 14 was obtained) is sharply peaked at the electron plasma frequency near 16.5 kHz. The broadening of the spectrum of electron plasma oscillations toward the higher frequency 31.1 kHz indicates that heating of the electron distribution began just before the rapid-sample measurement was taken, and occurs throughout the rapid-sample time interval. The five consecutive average

electric field spectra measured between 2220:00 and 2220:26 UT immediately after the rapid-sample measurement of the 31.1 kHz channel and corresponding with the main gradient of the magnetic field (see Figure 13) are shown in the lower panel of Figure 14. Each spectrum is labeled by a time-ordered snapshot number. The averaging time of snapshot 1 includes the foot of the magnetic field gradient. Snapshot 5 is the most intense electric field spectrum of the sequence and is defined as the shock electric field spectrum, similar to those shown in Figure 1. The development of the broad peak centered near the 3.11 kHz channel in snapshot 1 correlates with the appearance, in the leading edge of the shock, of 0.5 - 4.0 Hz whistler waves of the type reported by Fairfield [1974]. Further upstream, where the spectrum of electron plasma oscillations is sharply peaked at the electron plasma frequency near 16.5 kHz, the 0.5 - 4.0 Hz waves have damped out. These upstream whistler waves probably involve resonant interactions with electrons [Fairfield, 1974]. Therefore the broadening of the spectrum of electron plasma oscillations toward lower frequencies probably indicates scattering interactions between upstream electrons and the 0.5 - 4.0 Hz whistler waves. The overall broadening of the spectrum of electron plasma oscillations toward 31.1 kHz and 3.11 kHz thus clearly indicates the occurrence of electron heating in the leading edge of the shock and we interpret the peak at 3.11 kHz in snapshot 1 to mean that maximum heating of the electron distribution has occurred.

Following the sequence of snapshot numbers 1-5, it can be seen that as the main gradient of the magnetic field of the shock is traversed the electric field spectrum develops a peak at 311 Hz simultaneously with the disappearance of the peak at 3.11 kHz. Since proton heating in the bow shock is observed to occur after electron heating [Montgomery et al., 1970; Formisano and Hedgecock, 1973b], i.e., deeper within the shock transition region, we therefore conclude that the broad peak centered at 311 Hz in the shock spectrum corresponds to the occurrence of maximum proton heating. This broad peak of electrostatic turbulence in the shock spectrum is usually centered between 200 - 800 Hz, corresponds to $E_{rms,2}$ in the correlations of Table 3, and is characteristic of almost all shock crossings, as shown by the sample of shock spectra in Figure 1. Also characteristic of most bow shock crossings is the sequential development in electric field spectra through the shock transition shown by the snapshots 1-5 of Figure 14, which suggests that the electrostatic turbulence associated with the 3.11 kHz peak couples into lower frequencies during the proton heating process. It is interesting to note that this variation in electrostatic turbulence with frequency indicates that a strong coupling mechanism exists between the electron and proton heating processes in the bow shock since the direction of energy cascade in the spectrum of electrostatic turbulence is toward lower frequencies rather than toward higher frequencies as might be expected [Roth, 1971] in a turbulent spectrum analogous to conventional hydrodynamic turbulence. Past the downstream edge of the transition region the upper panel of

Figure 13 shows that the electrostatic turbulence at low frequencies decreases but still remains at an intensity that is large compared with the noise at higher frequencies. The resulting electric field spectrum in the near downstream region resembles the shock spectrum at a reduced intensity.

It can also be seen in Figure 13 that in the upstream region before about 2213 UT the GSFC magnetometer data shows the presence of long period (3-60 seconds) waves of the type which are thought to be generated by superthermal proton streams reflected from the bow shock [Greenstadt et al., 1968, 1970; Fairfield, 1969; Barnes, 1970; Scarf et al., 1970; Fredricks, 1975]. Scarf et al. [1970] have observed direct correlations between electrostatic oscillations at 3 kHz, associated with the ion plasma frequency in the solar wind, and the long period magnetic field oscillations. The top panel of Figure 13 shows that electrostatic oscillations at 31.1 kHz, associated with the electron plasma frequency, are also in direct correlation with the long period waves in the interplanetary magnetic field. The electrostatic oscillations at 31.1 kHz probably result from the electron stream that must accompany the reflected proton stream to provide charge neutralization.

VI. SUMMARY OF RESULTS AND CONCLUSIONS

The plasma wave turbulence of the earth's bow shock displays distinct correlations with several upstream solar wind parameters. It is found that the intensity variations of electrostatic turbulence in the bow shock correlates strongly with the ratio of electron to proton temperatures T_e/T_p and with the proton temperature T_p, as measured in the upstream solar wind. For large values of T_e/T_p, large values of the electrostatic r.m.s. field strength $E_{rms,2}$ occur, where $E_{rms,2}$ is obtained by integrating the shock electric field spectrum from 200 Hz to 4 kHz. The negative correlation found between $E_{rms,2}$ and T_p, implies that changes in the upstream proton temperature modulate the efficiency of the electrostatic turbulence mechanism which is associated with the value of T_e/T_p. If we make the plausible assumption that more intense levels of electrostatic turbulence occur when an unstable plasma is further removed from the threshold of stability, then we can relate the observed correlations of $E_{rms,2}$ with T_e/T_p and T_p to specific electrostatic wave modes whose stability criteria depend on T_e/T_p and T_p. Two-stream instability criteria are often expressed in terms of the two parameters T_e/T_i and v_d/v_e, where v_d is a relative drift velocity and v_e is the electron thermal speed [Stringer, 1964; Tidman and Krall, 1971, chap. 7]. A discussion of two-stream instability modes that are candidates for bow shock

turbulent heating mechanisms has been given by Greenstadt and Fredricks [1974], who derive stability criteria in terms of the minimum relative drift speed v_d between electrons and ions which must be exceeded over the scale length of the shock magnetic field gradient $\Delta B/B_o$ in order for instability to occur. Various scale lengths are chosen, all of which are proportional to T_e/T_i and/or β_i ($= 8\pi NKT_i/|\vec{B}|^2$). The temperature ratio T_e/T_i and the relative drift velocity v_d (or v_d/v_e) respectively indicate the relative widths of the electron and ion distribution functions and the relative displacement between the maximums of the two distributions. In terms of T_e/T_i and v_d the two-stream stability criteria indicate how well resolved from each other in velocity space the two streams have to be before unstable waves are generated. In general, anything that increases the resolution between the streams enhances the potential for instability and would be expected to lead to more intense levels of electrostatic turbulence. In particular, the positive correlation between $E_{rms,2}$ and T_e/T_p suggests that electrostatic turbulence in the bow shock is associated with a two-stream instability, the stability threshold of which is probably exceeded if T_e increases substantially in the leading edge of the bow shock. Electron preheating in the leading edge is confirmed by the broadening of the spectrum of electron plasma oscillations over the range of frequencies 3-30 kHz. For typical solar wind conditions only the electron distribution undergoes an appreciable drift in the bow shock gradient [Wu and Fredricks, 1972] so that the instability arises from electrons drifting through an ion background.

The result of this study that $E_{rms,2}$ has a strong negative correlation with the proton temperature T_p is consistent with an electron-proton streaming instability because for a given relative displacement v_d/v_e a smaller width to the proton distribution $f_p(v)$ contributes to better resolution of the two streams and an enhanced potential for instability. Thus, variations in T_p could serve to modulate the intensity of the resulting electrostatic turbulence.

As indicated by Greenstadt and Fredricks [1974], streaming between electron and proton distributions preferentially heats electrons, which corresponds to the observation of maximum electron heating occurring in the leading edge of the bow shock. To heat ions, the major dissipation mechanism of the bow shock, to temperatures such that $T_p \sim (2\text{-}4)T_e$ requires a streaming between ions [Auer et al., 1971; Papadopoulos, 1971; Biskamp and Welter, 1972], or other nonlinear instability modes. In the correlations of Table 3, $E_{rms,2}$ corresponds to the electrostatic turbulence observed in the main shock gradient and was identified with the maximum heating of protons. The strong correlation of $E_{rms,2}$ with T_e/T_p and T_p as measured upstream of the bow shock thus implies that the heating of protons in the main transition is strongly coupled to the heating of electrons in the leading edge of the shock. The coupling of the electron and proton heating mechanisms is most clearly shown by the characteristic sequential development of the electric field spectrum through the shock transition, an example of which is shown in Figure 14, in which the intensity of electrostatic turbulence at lower frequencies (~ 300 Hz) increases

simultaneously with a decrease in electrostatic turbulence at the higher frequencies associated with electron preheating. The low frequency (200-800 Hz) peak in the spectrum of electrostatic turbulence, associated with the maximum in proton heating, is characteristic of almost all shock electric field spectra.

Low frequency (20 Hz - 200 Hz) electric field turbulence, represented by $E_{rms,1}$ is found to correlate strongly with T_e/T_p and T_p, similar to the correlations of $E_{rms,2}$ with T_e/T_p and T_p, and therefore indicating that a substantial portion of the electric field energy density at low frequencies is derived from electrostatic waves. The entire electric field spectrum measured in the bow shock is thus primarily composed of electrostatic turbulence, and is associated with the occurrence of maximum proton heating. Since $E_{rms,1}$ also correlates with the shock normal angle $\psi(\vec{B},\hat{n})$, similar to the correlation of B_{rms} with $\psi(\vec{B},\hat{n})$, this is taken as evidence that $E_{rms,1}$ is also derived from the electric field of an electromagnetic mode, probably whistlers, which couples to electrostatic waves at frequencies below the electron gyrofrequency.

Electromagnetic turbulence in the bow shock, represented by the r.m.s. field strength of magnetic field fluctuations B_{rms} in the range 20 Hz - 4 kHz, is found to show positive correlations with the particle density N and the shock normal angle $\psi(\vec{B},\hat{n})$. These correlations are consistent with whistler turbulence with high density, perpendicular shocks having the largest values of B_{rms}. Upstream fluid parameters, such as M_A and β, used in the m.h.d. description of the

bow shock do not correlate with B_{rms}, presumably because the range of frequencies for B_{rms} covers only the high frequency, low spectral density portion of the total magnetic field spectrum near the bow shock.

ACKNOWLEDGMENTS

We would like to thank Drs. N. F. Ness and D. H. Fairfield for providing us with measurements of the magnetic field data, and Drs. S. J. Bame and W. C. Feldman for the solar wind particle data. This work was supported in part by the National Aeronautics and Space Administration under Contract NAS5-11074 and Grants NGL-16-001-002 and NGL-16-001-043 and by the Office of Naval Research under Grant N00014-68-A-0196-0009.

REFERENCES

Auer, P. L., R. W. Kilb, and W. F. Crevier, Thermalization in the earth's bow shock, J. Geophys. Res., 76, 2927, 1971.

Barnes, A., Theory of generation of bow-shock-associated hydromagnetic waves in the upstream interplanetary medium, Cosmic Electrodynamics, 1, 90, 1970.

Bevington, P. R., Data Reduction and Error Analysis for the Physical Sciences, McGraw-Hill, New York, 1969.

Biskamp, D., Ion sound turbulence in a collisionless shock wave, J. Geophys. Res., 75, 4659, 1970.

Biskamp, D. and H. Welter, Structure of the earth's bow shock, J. Geophys. Res., 77, 6052, 1972.

Biskamp, D., Collisionless shock waves in plasmas, Nucl. Fusion, 13, 719, 1973.

Fairfield, D. H., Bow shock associated waves observed in the far upstream interplanetary medium, J. Geophys. Res., 74, 3541, 1969.

Fairfield, D. H. and N. F. Ness, Magnetic field fluctuations in the earth's magnetosheath, J. Geophys. Res., 75, 6050, 1970.

Fairfield, D. H., Average and unusual locations of the earth's magnetopause and bow shock, J. Geophys. Res., 76, 6700, 1971.

Fairfield, D. H., Whistler waves observed upstream from collisionless shocks, J. Geophys. Res., 79, 1368, 1974.

Formisano, V. and C. F. Kennel, Small amplitude waves in high β plasmas, J. Plasma Phys., 3, 55, 1969.

Formisano, V. and P. C. Hedgecock, Solar wind interaction with the earth's magnetic field, 3, On the earth's bow shock structure, J. Geophys. Res., 78, 3745, 1973a.

Formisano, V. and P. C. Hedgecock, On the structure of the turbulent bow shock, J. Geophys. Res., 78, 6522, 1973b.

Formisano, V. and G. Moreno, Relationships among the interplanetary plasma parameters: Heos 1, December 1968 to December 1969, J. Geophys. Res., 79, 5109, 1974.

Fredricks, R. W., C. F. Kennel, F. L. Scarf, G. M. Crook, and I. M. Green, Detection of electric-field turbulence in the earth's bow shock, Phys. Rev. Lett., 21, 1761, 1968.

Fredricks, R. W., F. V. Coroniti, C. F. Kennel, and F. L. Scarf, Fast time-resolved spectra of electrostatic turbulence in the earth's bow shock, Phys. Rev. Lett., 24, 994, 1970a.

Fredricks, R. W., G. M. Crook, C. F. Kennel, I. M. Green, and F. L. Scarf, OGO 5 observations of electrostatic turbulence in bow shock magnetic structures, J. Geophys. Res., 75, 3751, 1970b.

Fredricks, R. W., A model for generation of bow-shock-associated upstream waves, J. Geophys. Res., 80, 7, 1975.

Greenstadt, E. W., I. M. Green, G. T. Inouye, A. J. Hundhausen, S. J. Bame, and I. B. Strong, Correlated magnetic field and plasma observations of the earth's bow shock, J. Geophys. Res., 73, 51, 1968.

Greenstadt, E. W., I. M. Green, G. T. Inouye, D. S. Colburn, J. H. Binsack, and E. F. Lyon, Dual satellite observation of the earth's bow shock, 2, Field-aligned upstream waves, Cosmic Electrodynamics, 1, 279, 1970.

Greenstadt, E. W., Structure of the terrestrial bow shock, in Solar Wind Three, edited by C. T. Russell, p. 440, Institute of Geophysics and Planetary Physics, University of California, Los Angeles, 1974.

Greenstadt, E. W. and R. W. Fredricks, Plasma instability modes related to the earth's bow shock, in Magnetospheric Physics, ed. by B. M. McCormac, p. 355, D. Reidel, Dordrecht, Holland, 1974.

Greenstadt, E. W., C. T. Russell, F. L. Scarf, V. Formisano, and M. Neugebauer, Structure of the quasi-perpendicular laminar bow shock, J. Geophys. Res., 80, 502, 1975.

Holzer, R. E., M. G. McLeod, and E. J. Smith, Preliminary results from the OGO 1 search coil magnetometer: Boundary positions and magnetic noise spectra, J. Geophys. Res., 71, 1481, 1966.

Holzer, R. E., T. G. Northrup, J. V. Olson, and C. T. Russell, Study of waves in the earth's bow shock, J. Geophys. Res., 77, 2264, 1972.

Montgomery, M. D., J. R. Asbridge, and S. J. Bame, Vela 4 plasma observation near the earth's bow shock, J. Geophys. Res., 75, 1217, 1970.

Neugebauer, M., Initial deceleration of solar wind positive ions in the earth's bow shock, J. Geophys. Res., 75, 717, 1970.

Neugebauer, M., C. T. Russell, and J. V. Olson, Correlated observations of electrons and magnetic fields at the earth's bow shock, J. Geophys. Res., 76, 4366, 1971.

Neville, A. M. and J. B. Kennedy, Basic Statistical Methods, International Textbook Company, Scranton, Pennsylvania, 1964.

Olson, J. V., R. E. Holzer, and E. J. Smith, High-frequency magnetic fluctuations associated with the earth's bow shock, J. Geophys. Res., 74, 4601, 1969.

Paul, J. W. M., Collisionless shocks, in Cosmic Plasma Physics, ed. by K. Schindler, p. 293, Plenum Press, New York-London, 1972.

Papadopoulos, K., Ion thermalization in the earth's bow shock, J. Geophys. Res., 76, 3806, 1971.

Rodriguez, P. and D. A. Gurnett, Electrostatic and electromagnetic turbulence associated with the earth's bow shock, J. Geophys. Res., 80, 19, 1975.

Roth, J. R., Experimental study of spectral index, mode coupling, and energy cascading in a turbulent, hot-ion plasma, Phys. Fluids, 14, 2193, 1971.

Scarf, F. L., R. W. Fredricks, L. A. Frank, C. T. Russell, P. J. Coleman, Jr., and M. Neugebauer, Direct correlations of large-amplitude waves with suprathermal protons in the upstream solar wind, J. Geophys. Res., 75, 7316, 1970.

Stringer, T. E., Electrostatic instabilities in current-carrying and counterstreaming plasmas, Plasma Phys., J. Nucl. Energy, C6, 267, 1964.

Tidman, D. A., and N. A. Krall, Shock Waves in Collisionless Plasmas, John-Wiley-Interscience, New York, 1971.

Woods, L. C., Critical Alfven-Mach numbers for transverse field mhd shocks, Plasma Phys., 11, 25, 1969a.

Woods, L. C., On the structure of collisionless magneto-plasma shock waves of super-critical Alfven-Mach numbers, J. Plasma Phys., 3, 435, 1969b.

Woods, L. C., On double-structured, perpendicular magneto-plasma shock waves, Plasma Phys., 13, 289, 1971.

Wu, C. S. and R. W. Fredricks, Cyclotron drift instability in the bow shock, J. Geophys. Res., 77, 5585, 1972.

Table 1

Solar Wind Parameter Characteristics

	Min	Max	Mean	Standard Deviation
M_A	1.5	26.6	6.8	4.7
β	0.03	4.5	1.02	0.87
$\lvert\vec{B}\rvert$ (γ)	2.0	16.9	7.5	3.2
M_s	3.9	12.5	7.8	1.9
C_s (km/s)	33.2	105.	58.	14.
N (cm^{-3})	0.5	19.0	5.2	3.4
C_A	15.4	278.	88.	60.
$\psi(\vec{B},\hat{n})$ (deg)	11.7	90.	60.	19.
T_e/T_p	0.65	9.0	2.6	1.8
V_{SW} (km/s)	315.	660.	431.	63.
T_e ($\times 10^5$ °K)	0.6	6.0	1.6	0.80
T_p ($\times 10^5$ °K)	0.15	3.0	0.98	0.72

Table 2

Energy Density Characteristics

	Min	Max	Mean*	Standard Deviations*	
$\epsilon(E_{rms,1})/\epsilon(SW)$ ($\times 10^{-8}$)	0.0028	6.4	0.17	0.021	1.3
$\epsilon(E_{rms,2})/\epsilon(SW)$ ($\times 10^{-8}$)	0.0001	14.2	0.054	0.0047	0.63
$\epsilon(B_{rms})/\epsilon(SW)$ ($\times 10^{-6}$)	0.026	5.9	0.38	0.10	1.4
$\epsilon(E_{rms,1})$ ($\times 10^{-19}$ ergs cm^{-3})	3.7	3020.	105.	16.	672.
$\epsilon(E_{rms,2})$ ($\times 10^{-19}$ ergs cm^{-3})	0.32	6120.	34.	2.9	400.
$\epsilon(B_{rms})$ ($\times 10^{-16}$ ergs cm^{-3})	1.1	2600.	24.	5.0	115.
$\epsilon(SW)$ ($\times 10^{-10}$ ergs cm^{-3})	6.9	440.	59.	22.	161.

*Logarithmic means and standard deviations

Table 3

Correlation Coefficients R

x \ y	$E_{rms,1}$ (20 Hz - 200 Hz)		$E_{rms,2}$ (200 Hz - 4 kHz)		B_{rms} (20 Hz - 4 kHz)	
M_A		-0.294		-0.300		0.149
β		-0.286		-0.266		0.150
C_A		0.286		0.136		-0.103
$\psi(\vec{B},\hat{n})$		0.342		0.141		0.386
$\lvert\vec{B}\rvert$		0.306		0.165		0.342
M_s	0.186		0.236		0.131	
Te/Tp	0.416		0.599		-0.110	
V_{sw}	-0.165		-0.361		0.300	
C_s	-0.328		-0.463		0.040	
N	0.032		0.242		0.500	
Te	-0.200		-0.241		-0.117	
Tp	-0.376		-0.566		0.185	
S	81	96	75	90	82	98
R_c(1%)	0.281	0.259	0.292	0.267	0.280	0.257

Fitted equation: $\log y = bx + a$

$$M_A = \frac{V_{sw}}{C_A} \qquad M_s = \frac{V_{sw}}{C_s} \qquad \beta = \frac{8\pi NK(Te+Tp)}{|\vec{B}|^2}$$

$$C_A = \frac{|\vec{B}|}{(4\pi N m_p)^{1/2}} \qquad C_s = \left[\frac{5}{3}\frac{K}{m_p}(T_e + T_p)\right]^{1/2}$$

FIGURE CAPTIONS

Figure 1 The intensity variability of bow shock electric field turbulence is indicated by the representative sample of shock spectra obtained in 36 crossings of the bow shock. The average spectra are 5.12 seconds averages and the peak spectra are 0.1 second averages. E_{rms} is the r.m.s. electric field strength obtained by integrating a given spectrum from 20 Hz to 200 kHz.

Figure 2 The intensity variability of bow shock magnetic field turbulence is represented by average and peak spectra obtained at the same 36 shock crossings of Figure 1. B_{rms} is the r.m.s. magnetic field strength.

Figure 3 The distributions of values for solar wind parameters used in the present study. The mean and standard deviations for each distribution are indicated by the dot and error bars, respectively.

Figure 4 The distributions of values for solar wind parameters used in the present study, similar to Figure 3. Means and standard deviations indicated as in Figure 3.

Figure 5 The distributions of the ratios of plasma wave energy densities to the solar wind energy density. The logarithmic mean values and standard deviations of the ratios are indicated on the plots.

Figure 6 The distributions of the absolute values of plasma wave energy densities and solar wind energy density.

Figure 7 The plot of $E_{rms,2}$ the r.m.s. field strength of the electrostatic component of the shock spectrum (200 Hz - 4 kHz), against T_e/T_p which shows a strong positive correlation. The dashed diagonal line is the line of regression for a least squares fit to the equation $\log y = bx + a$, where $y = E_{rms,2}$ and $x = T_e/T_p$. The slope of the regression line, which is the important meausre of association, has a dispersion which is indicated by rotating the regression line about its centroid to the limits indicated by the small error bars at $\pm 2.576\ \sigma(\bar{y})$. The large error bars at $\pm\ \sigma(y)$ probably arise from short period fluctuations in T_e/T_p and from correlations with other upstream parameters not considered in this two-parameter fit.

Figure 8 The plot of $E_{rms,2}$ against the upstream proton temperature T_p showing a strong negative correlation for a least squares fit to log y = bx + a where $y = E_{rms,2}$ and $x = T_p$. The error bars have the same meaning as in Figure 7.

Figure 9 The plot of $E_{rms,1}$ against T_e/T_p which indicates a positive correlation. $E_{rms,1}$ is the r.m.s. field strength of the electric field between 20 Hz and 200 Hz in the shock spectrum, and is observed to correlate with T_e/T_p similarly to the correlation shown in Figure 7 between $E_{rms,2}$ and T_e/T_p. The error bars have the same meaning as in the two previous figures.

Figure 10 The plot of B_{rms}, the r.m.s. magnetic field strength of the electromagnetic component of the shock spectrum (20 Hz - 4 kHz), against the solar wind particle density N. A positive correlation is indicated. The error bars have the same meaning as in previous figures.

Figure 11 The plot of B_{rms} against the shock normal angle $\psi(\vec{B},\hat{n})$, showing a positive correlation. The error bars have the same meaning as in previous figures.

Figure 12 Rapid-sample measurement of the electric field at 3.11 kHz showing the correlation with the transition region as determined by the magnetic field. The interval between the vertical dashed lines ⓐ and ⓑ indicates the leading edge of the shock where the initial electrostatic noise occurs. The main transition region, between ⓑ and ⓒ, corresponds to the large gradient in the magnetic field and the associated electrostatic turbulence. the intervals ⓐ - ⓑ and ⓑ - ⓒ probably correspond, respectively, to the regions of maximum electron and proton heating. Downstream fluctuations in electrostatic noise display an exponential damping which may result from further proton heating. The apparent periodicity of the major downstream fluctuations is not related to the spacecraft spin period so it may be assumed that the fluctuations are real time variations. Shock parameters: $M_A = 4.8$, $\beta = 0.28$, $T_e/T_p = 6.7$, $\psi(\vec{B},\hat{n}) = 87°$.

Figure 13 A shock crossing which shows the relation between the rise and relaxation times of electric field turbulence at high and low frequencies. Electric field noise is clearly detected ahead of the main gradient in the magnetic field. The solid vertical lines indicate the time intervals for the rapid-sample measurement and

electric field spectra of Figure 14. Upstream electrostatic oscillations at 3.11 kHz and 31.1 kHz are correlated with the long period waves in the magnetic field. Shock parameters: $M_A = 6.9$, $\beta = 1.42$, $T_e/T_p = 1.0$, $\psi(\vec{B},\hat{n}) = 90°$.

Figure 14 The polar plot is a rapid-sample measurement plotted versus the spacecraft spin angle in the solar ecliptic plane, and represents the electrostatic turbulence at 31.1 kHz in the leading edge of the shock crossing in Figure 13. The orientation of the upstream magnetic field vector is indicated by ϕ_B. The major principle axis of the distribution of rapid-sample measurements is indicated by ϕ_P. The electric field spectra in the lower panel indicate the sequential development of electrostatic turbulence with frequency as the main transition is traversed.

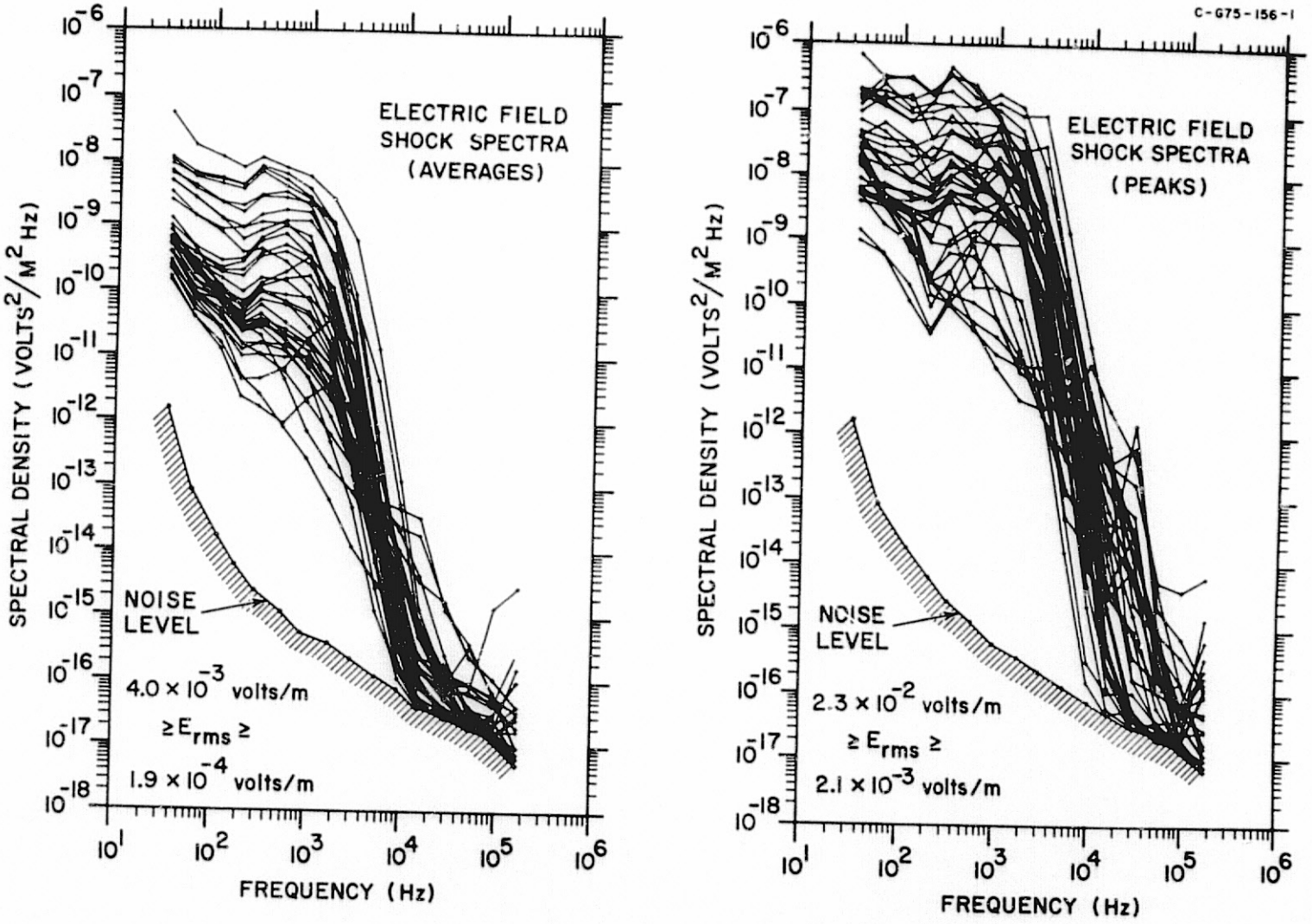
ELECTRIC FIELD
SHOCK SPECTRA
(AVERAGES)
NOISE
LEVEL
4.0 × 10^-3 volts/m
≥ E_rms ≥
1.9 × 10^-4 volts/m
SPECTRAL DENSITY (VOLTS²/M² Hz)
FREQUENCY (Hz)
C-G75-156-1
ELECTRIC FIELD
SHOCK SPECTRA
(PEAKS)
NOISE
LEVEL
2.3 × 10^-2 volts/m
≥ E_rms ≥
2.1 × 10^-3 volts/m
SPECTRAL DENSITY (VOLTS²/M² Hz)
FREQUENCY (Hz)

Figure 1

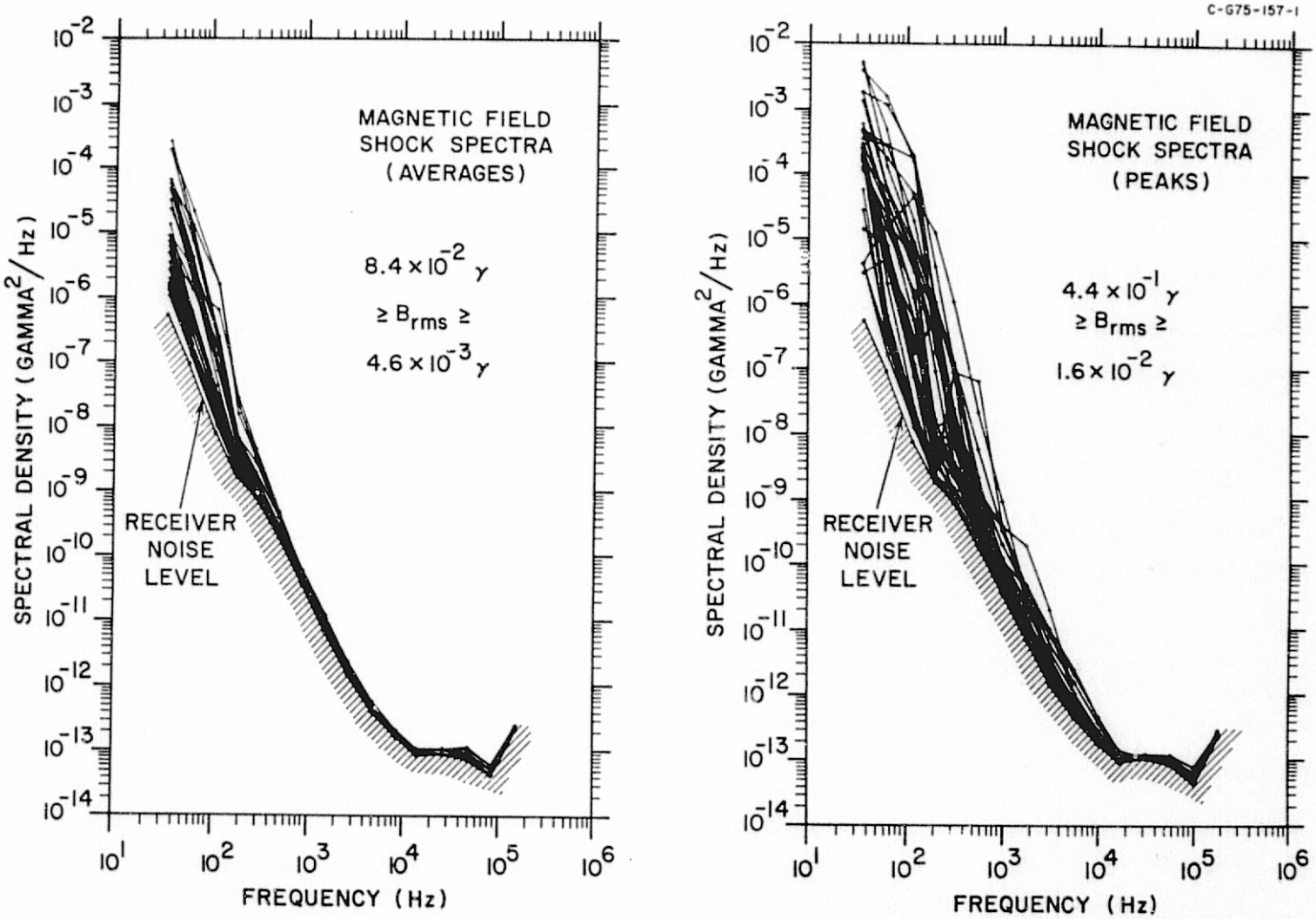
C-G75-157-1
MAGNETIC FIELD
SHOCK SPECTRA
(AVERAGES)
8.4 × 10^-2 γ
≥ B_rms ≥
4.6 × 10^-3 γ
RECEIVER
NOISE
LEVEL
SPECTRAL DENSITY (GAMMA^2/Hz)
FREQUENCY (Hz)
MAGNETIC FIELD
SHOCK SPECTRA
(PEAKS)
4.4 × 10^-1 γ
≥ B_rms ≥
1.6 × 10^-2 γ
RECEIVER
NOISE
LEVEL
SPECTRAL DENSITY (GAMMA^2/Hz)
FREQUENCY (Hz)

Figure 2

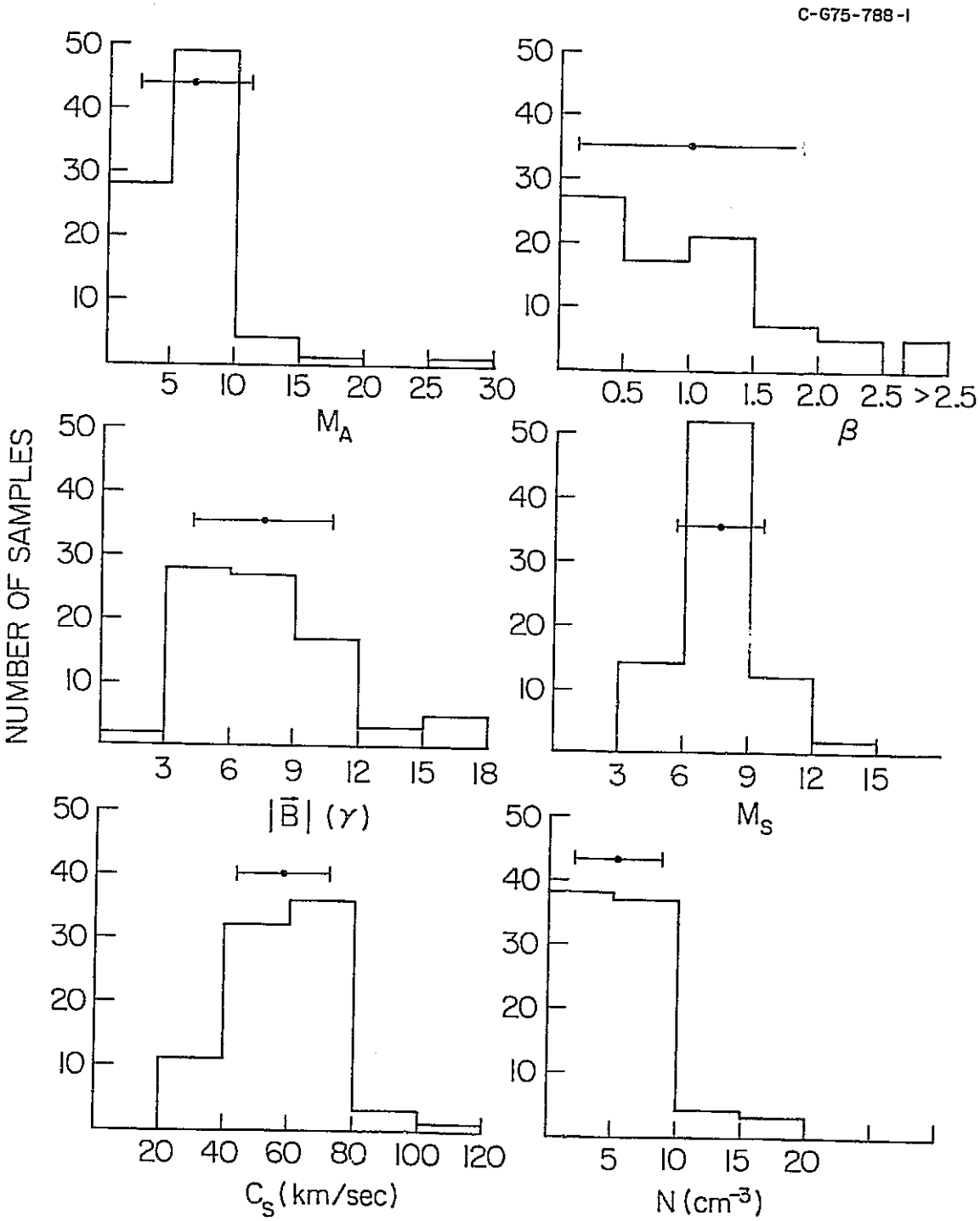
C-G75-788-I
NUMBER OF SAMPLES
50
40
30
20
10
5 10 15 20 25 30
M_A
0.5 1.0 1.5 2.0 2.5 >2.5
β
3 6 9 12 15 18
$|\vec{B}|$ (γ)
3 6 9 12 15
M_S
20 40 60 80 100 120
C_s (km/sec)
5 10 15 20
N (cm^{-3})

Figure 3

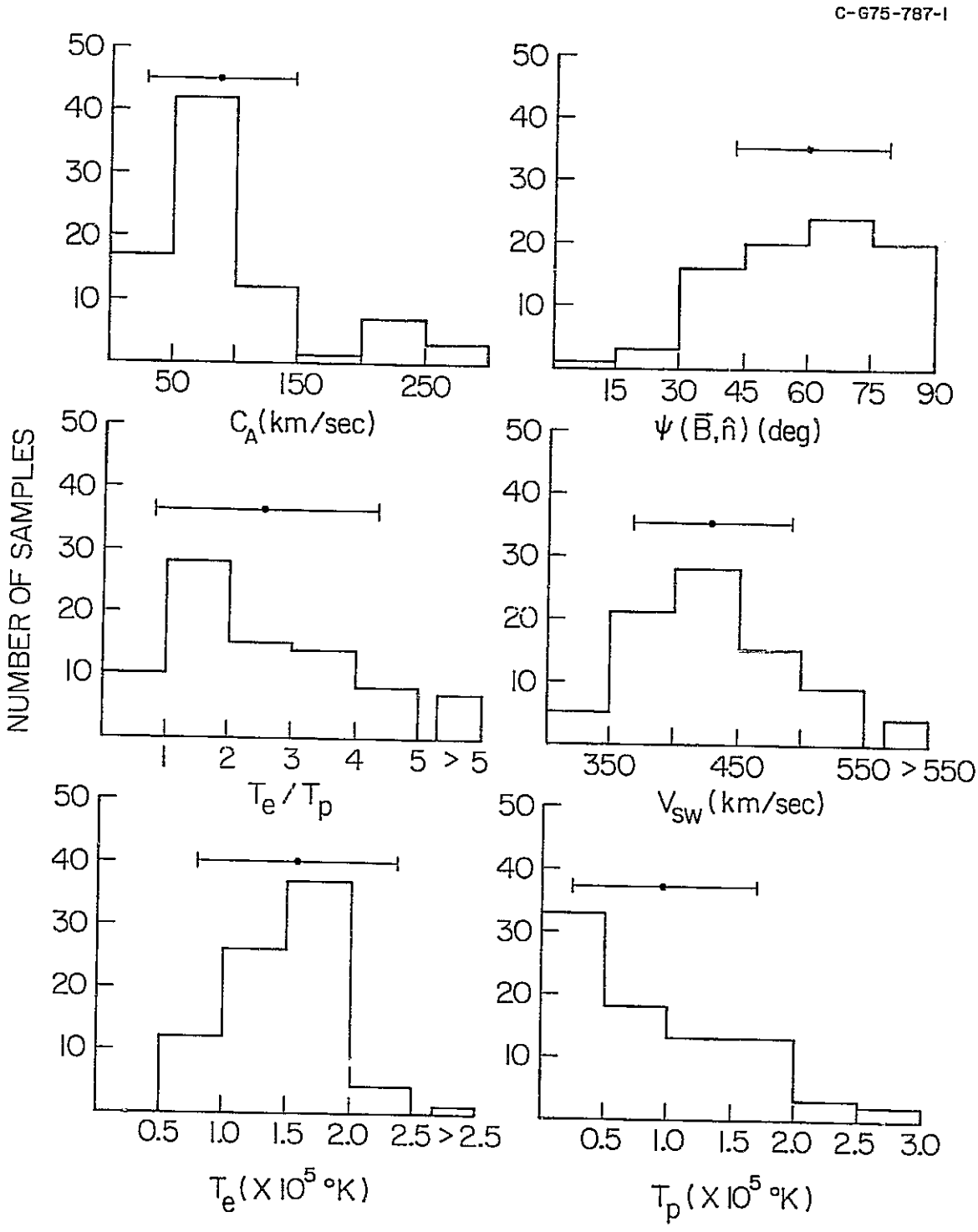
C-G75-787-I
NUMBER OF SAMPLES
50
40
30
20
10
50
150
250
C_A(km/sec)
15
30
45
60
75
90
$\psi(\vec{B},\hat{n})$ (deg)
1
2
3
4
5
>5
T_e/T_p
350
450
550
>550
V_{sw} (km/sec)
0.5
1.0
1.5
2.0
2.5
>2.5
T_e (X 10^5 °K)
3.0
T_p (X 10^5 °K)

Figure 4

C-G75-786-1

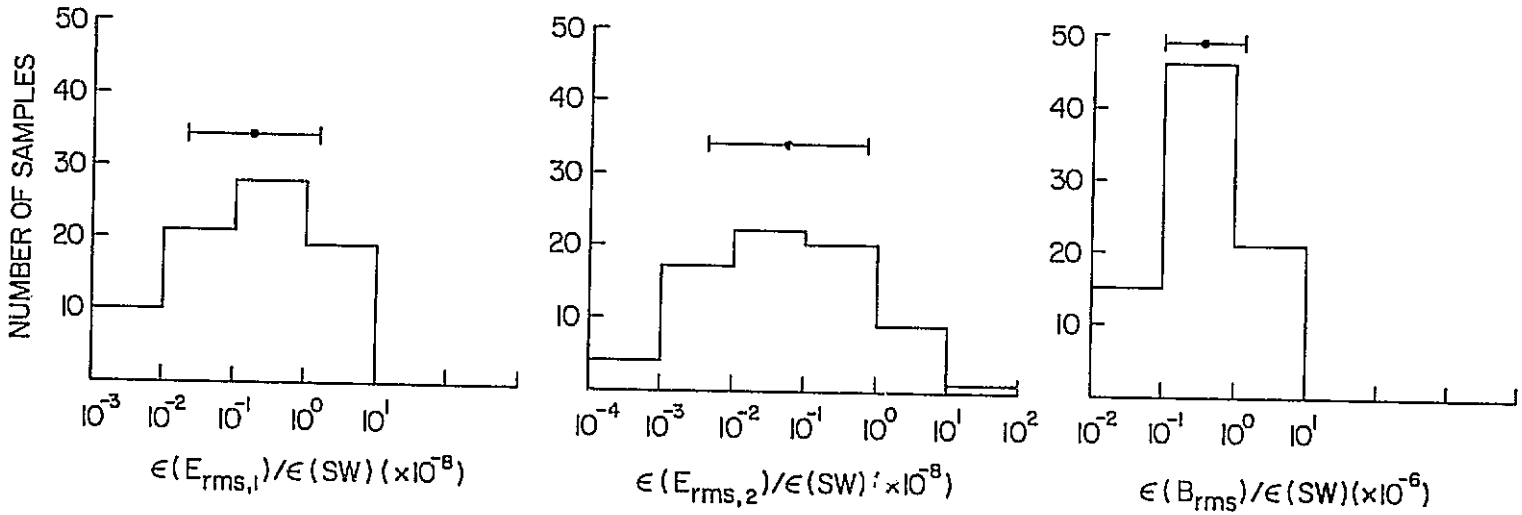

Figure 5

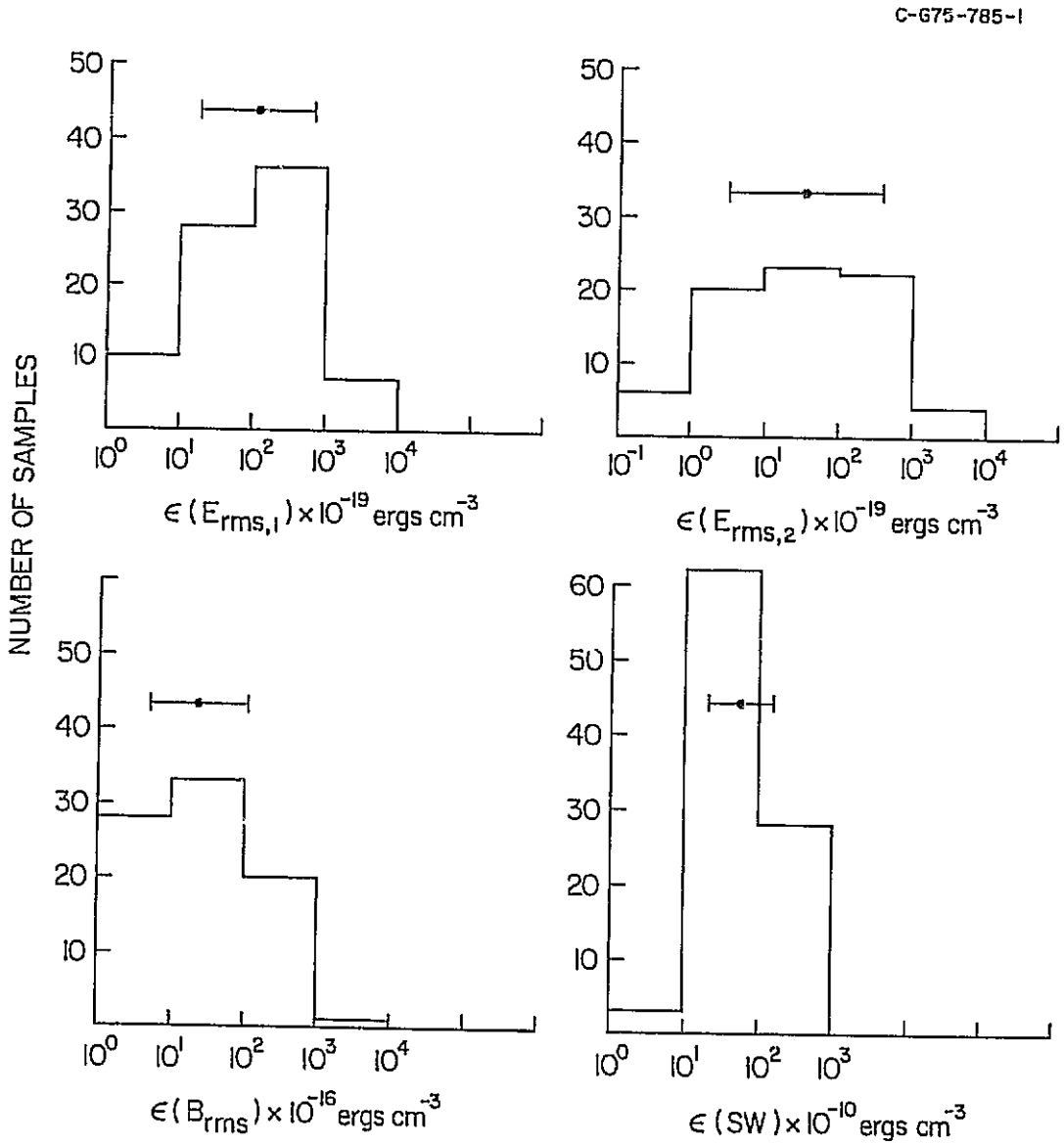
C-G75-785-1
NUMBER OF SAMPLES
50
40
30
20
10
10^0 10^1 10^2 10^3 10^4
$\epsilon(E_{rms,1}) \times 10^{-19}$ ergs cm^{-3}
10^{-1} 10^0 10^1 10^2 10^3 10^4
$\epsilon(E_{rms,2}) \times 10^{-19}$ ergs cm^{-3}
$\epsilon(B_{rms}) \times 10^{-16}$ ergs cm^{-3}
60
10^0 10^1 10^2 10^3
$\epsilon(SW) \times 10^{-10}$ ergs cm^{-3}

Figure 6

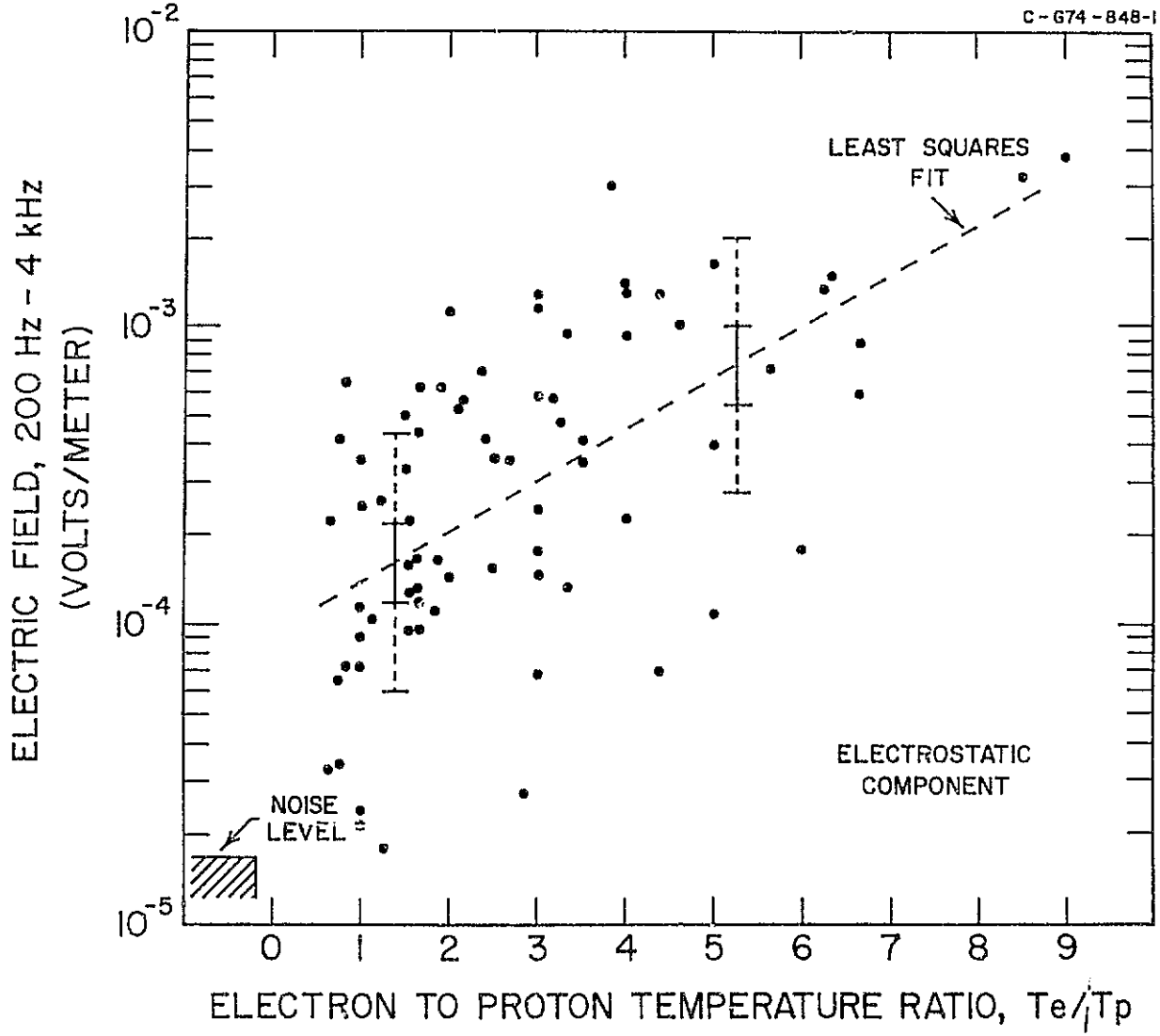
C-G74-848-I
ELECTRIC FIELD, 200 Hz - 4 kHz (VOLTS/METER)
10^{-2}
10^{-3}
10^{-4}
10^{-5}
LEAST SQUARES FIT
ELECTROSTATIC COMPONENT
NOISE LEVEL
0 1 2 3 4 5 6 7 8 9
ELECTRON TO PROTON TEMPERATURE RATIO, Te/Tp

Figure 7

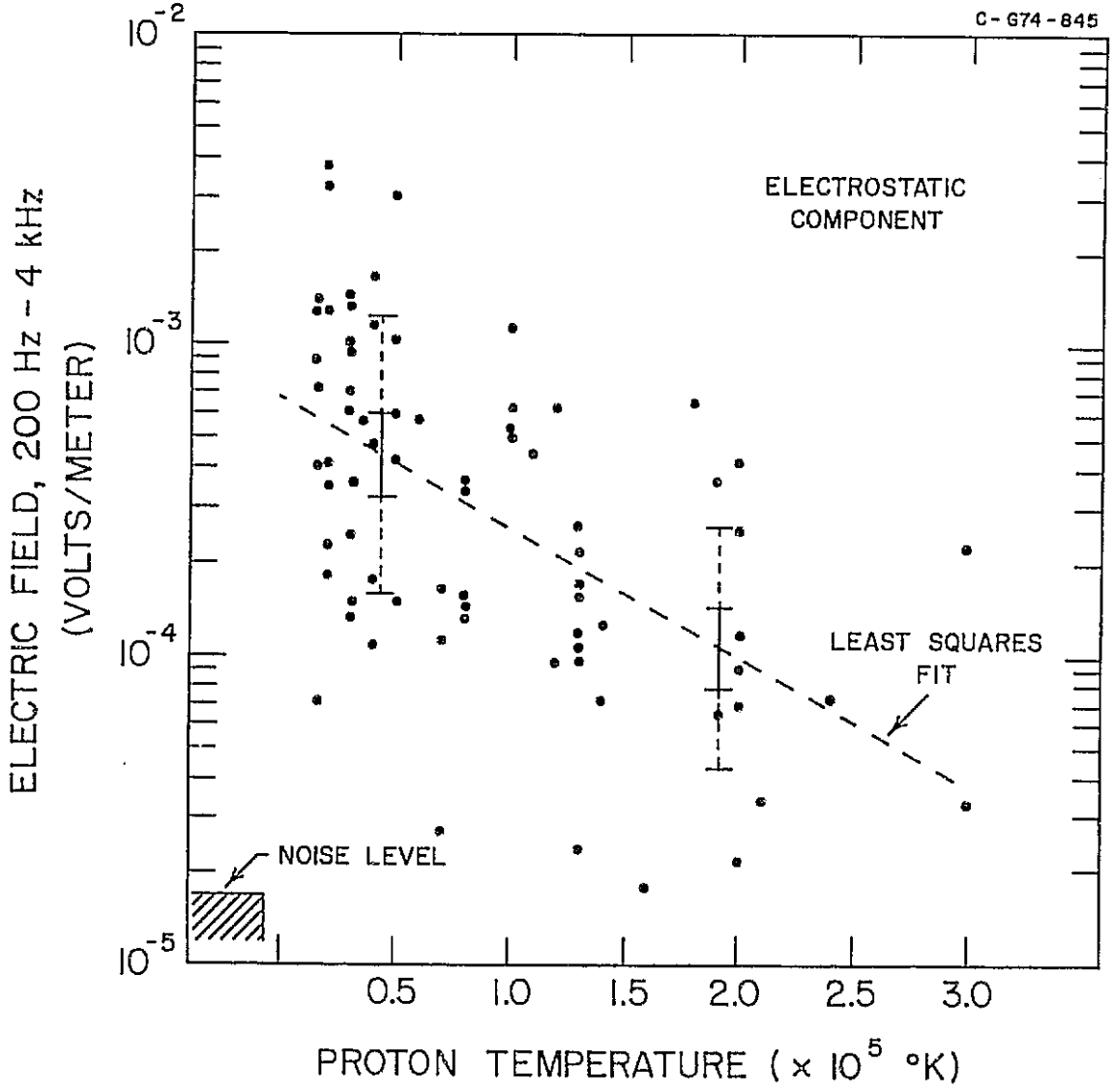
C-G74-845
ELECTRIC FIELD, 200 Hz - 4 kHz (VOLTS/METER)
10^{-2}
10^{-3}
10^{-4}
10^{-5}
ELECTROSTATIC COMPONENT
LEAST SQUARES FIT
NOISE LEVEL
0.5
1.0
1.5
2.0
2.5
3.0
PROTON TEMPERATURE (x 10^5 °K)

Figure 8

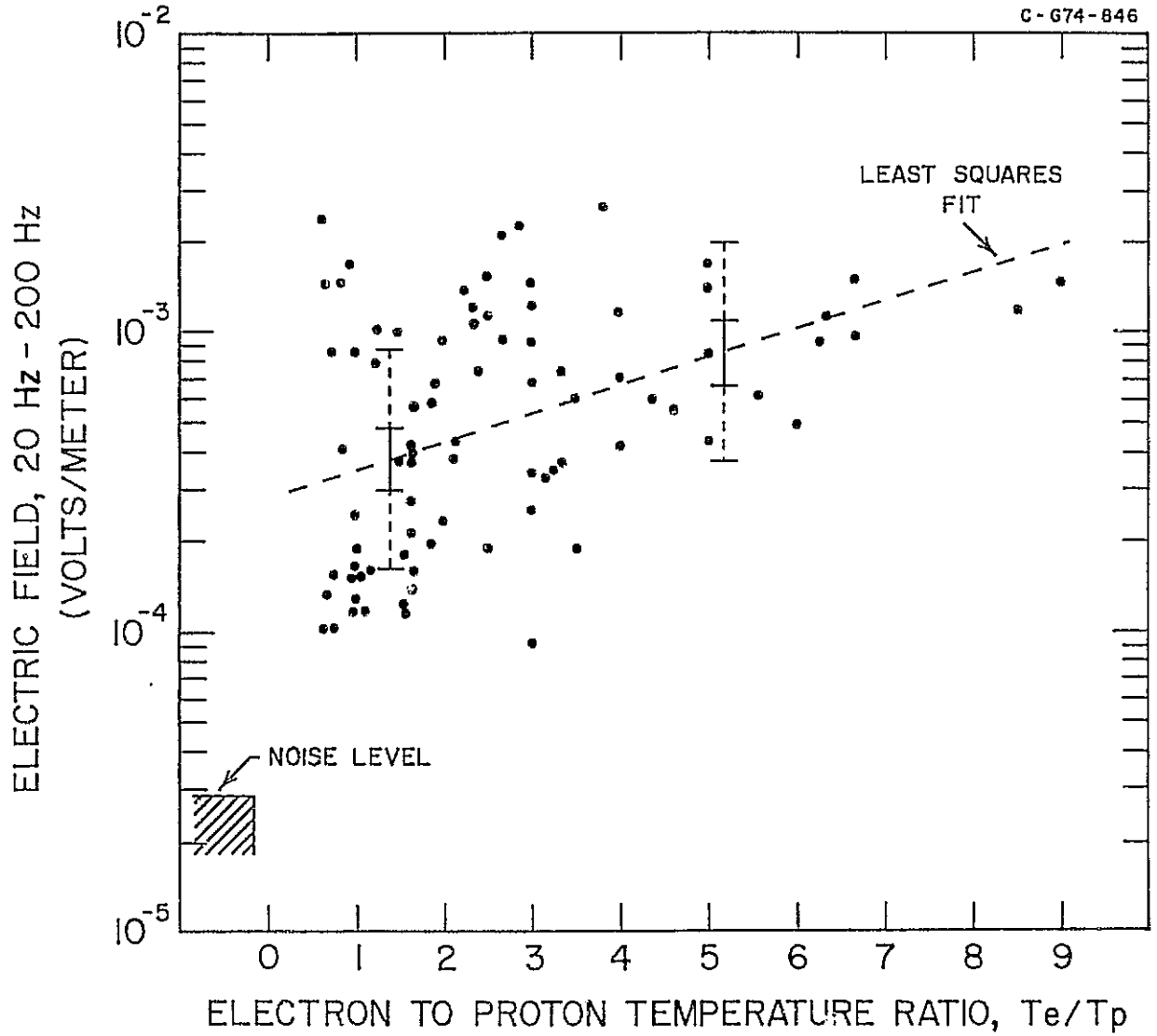
C-G74-846
ELECTRIC FIELD, 20 Hz - 200 Hz
(VOLTS/METER)
10^{-2}
10^{-3}
10^{-4}
10^{-5}
LEAST SQUARES
FIT
NOISE LEVEL
0 1 2 3 4 5 6 7 8 9
ELECTRON TO PROTON TEMPERATURE RATIO, Te/Tp

Figure 9

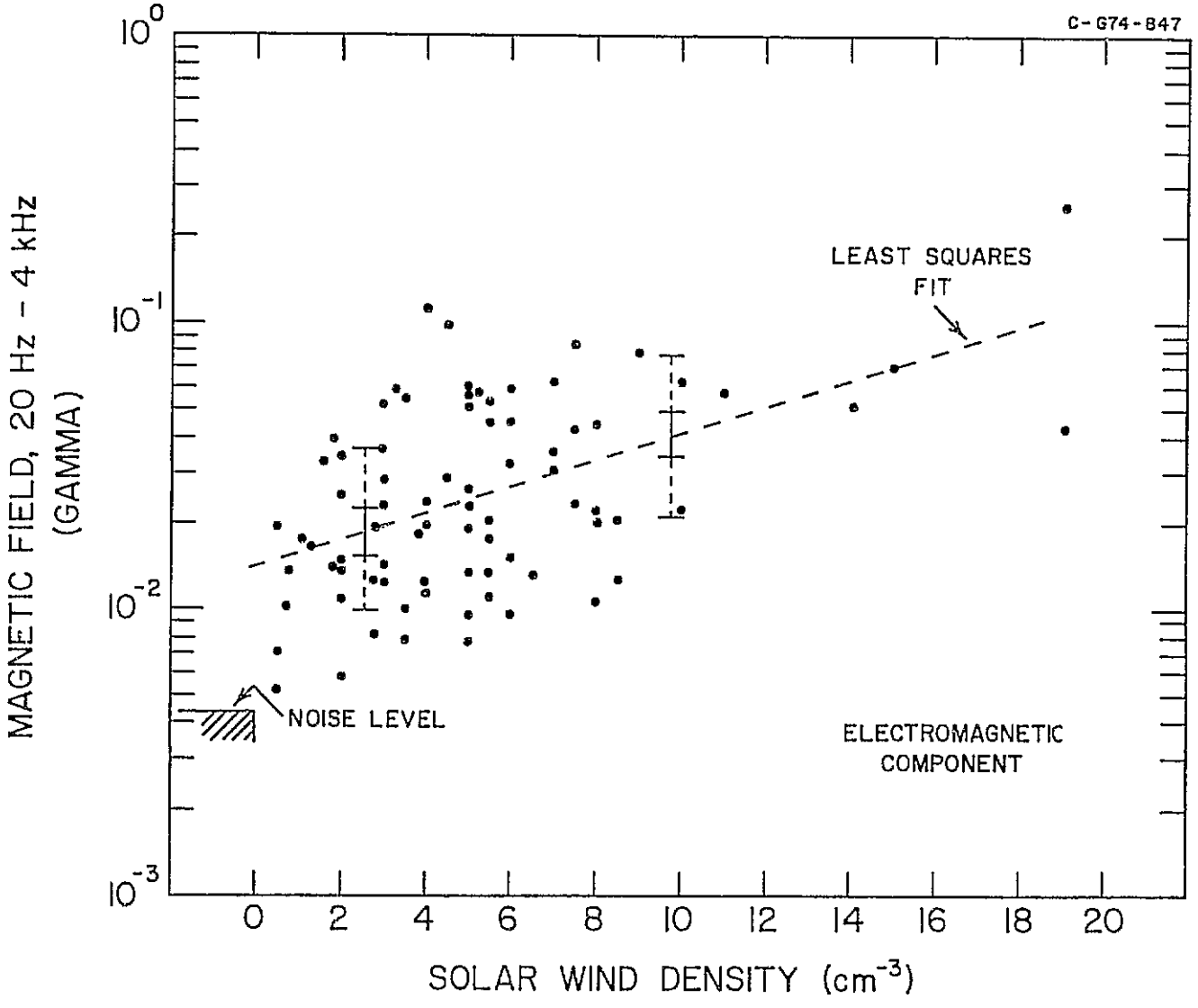
C-G74-847
MAGNETIC FIELD, 20 Hz - 4 kHz (GAMMA)
10^0
10^{-1}
10^{-2}
10^{-3}
LEAST SQUARES FIT
NOISE LEVEL
ELECTROMAGNETIC COMPONENT
0 2 4 6 8 10 12 14 16 18 20
SOLAR WIND DENSITY (cm^{-3})

Figure 10

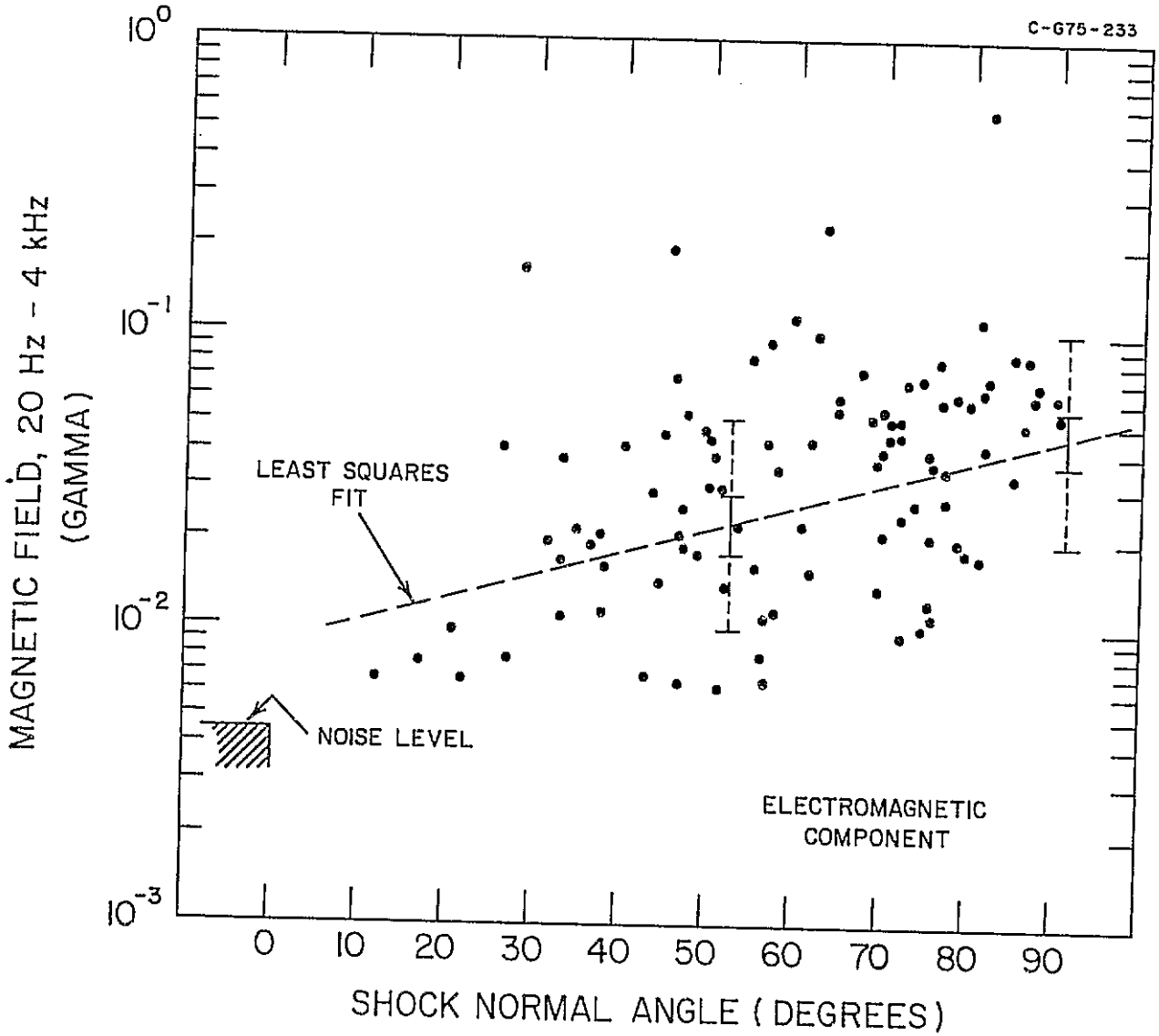
C-G75-233
MAGNETIC FIELD, 20 Hz - 4 kHz (GAMMA)
10^{0}
10^{-1}
10^{-2}
10^{-3}
LEAST SQUARES FIT
NOISE LEVEL
ELECTROMAGNETIC COMPONENT
0
10
20
30
40
50
60
70
80
90
SHOCK NORMAL ANGLE (DEGREES)

Figure 11

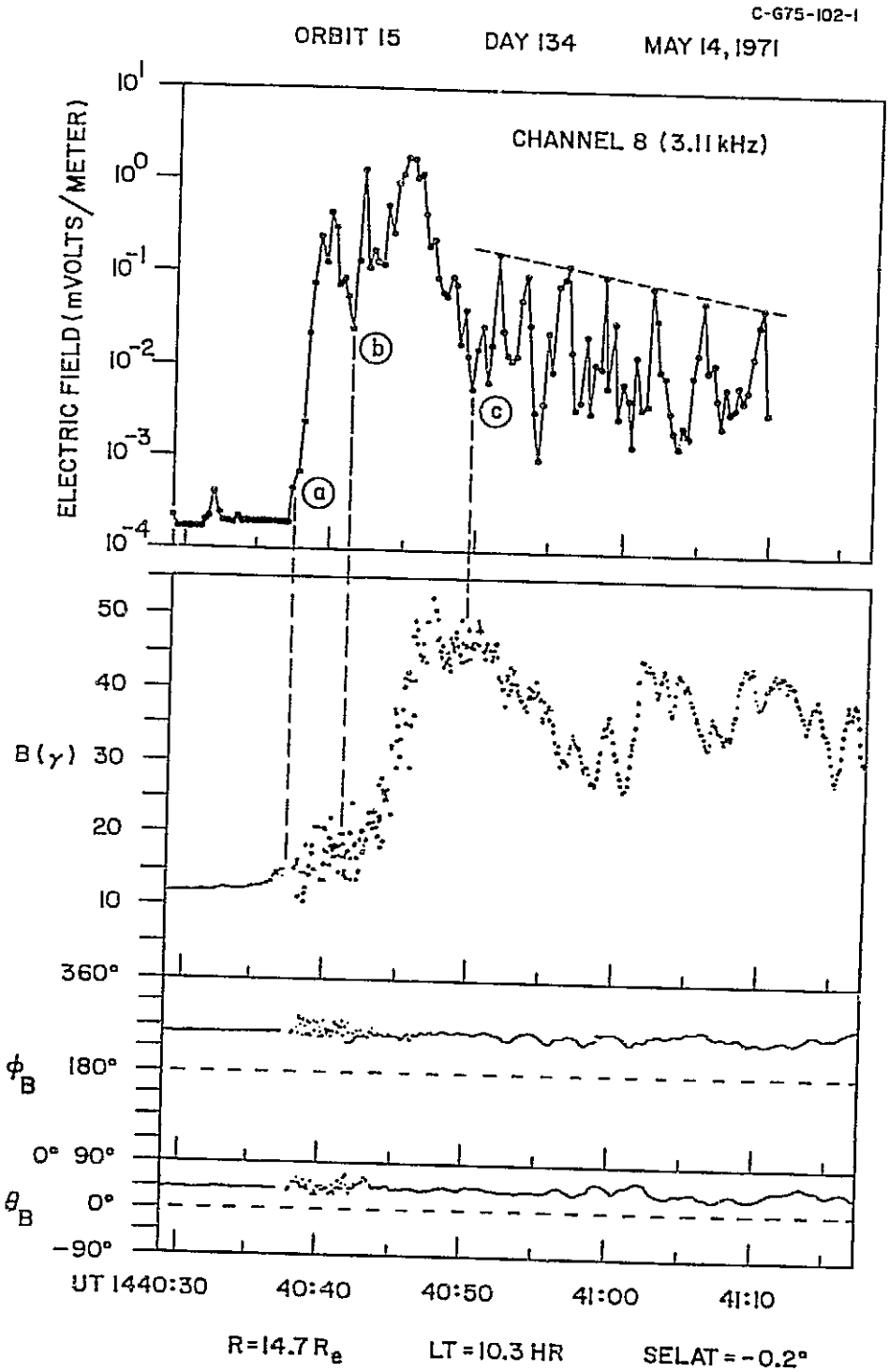
C-G75-102-1
ORBIT 15
DAY 134
MAY 14, 1971
CHANNEL 8 (3.11 kHz)
ELECTRIC FIELD (mVOLTS/METER)
10^{1}
10^{0}
10^{-1}
10^{-2}
10^{-3}
10^{-4}
a
b
c
B(γ)
50
40
30
20
10
360°
ϕ_B
180°
0°
90°
θ_B
0°
−90°
UT 1440:30
40:40
40:50
41:00
41:10
R=14.7 R_e
LT=10.3 HR
SELAT=−0.2°

Figure 12

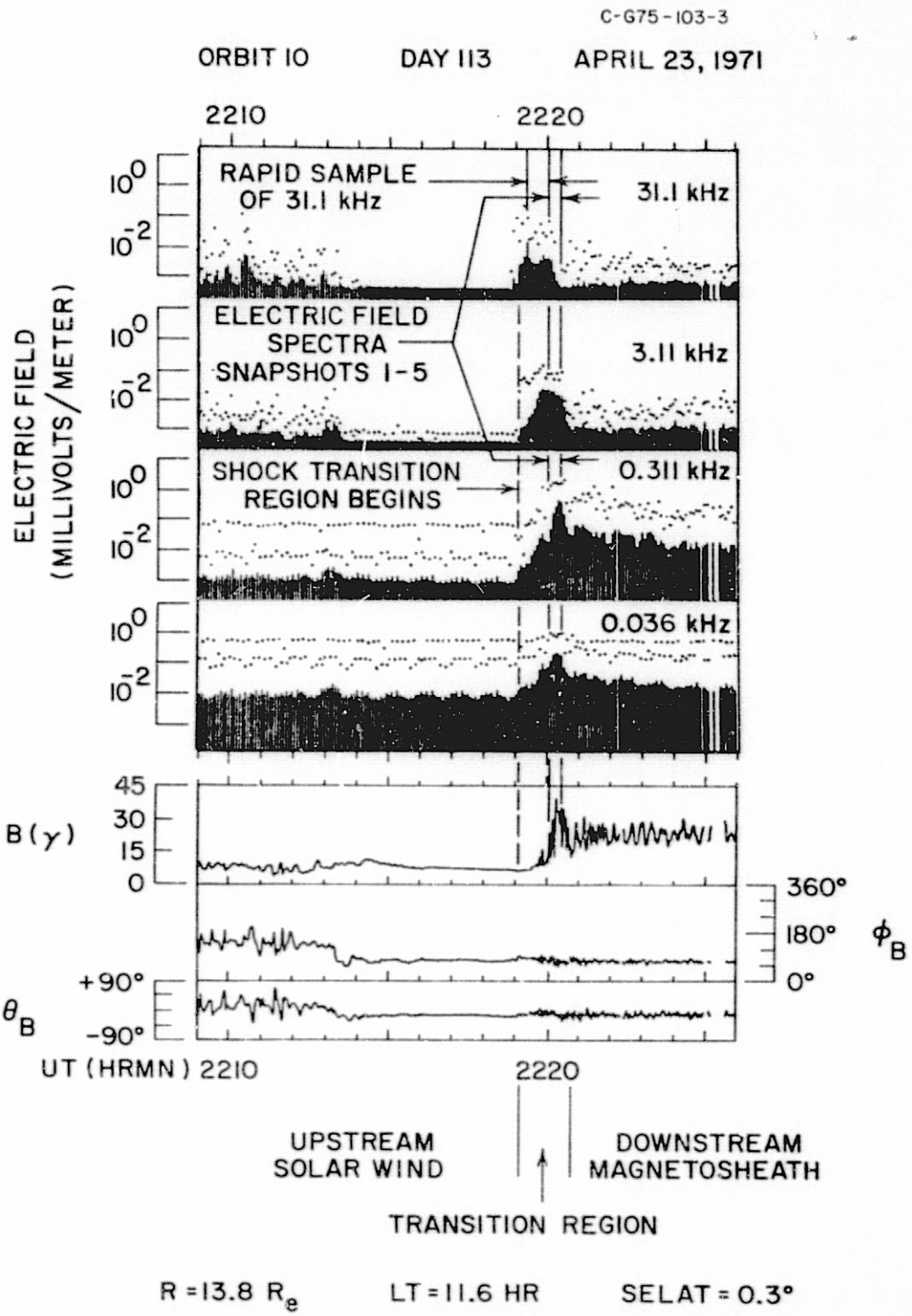
C-G75-103-3
ORBIT 10
DAY 113
APRIL 23, 1971
2210
2220
ELECTRIC FIELD (MILLIVOLTS/METER)
RAPID SAMPLE OF 31.1 kHz
31.1 kHz
ELECTRIC FIELD SPECTRA SNAPSHOTS 1-5
3.11 kHz
SHOCK TRANSITION REGION BEGINS
0.311 kHz
0.036 kHz
B(γ)
45
30
15
0
360°
180°
0°
ϕ_B
+90°
-90°
θ_B
UT (HRMN) 2210
2220
UPSTREAM SOLAR WIND
DOWNSTREAM MAGNETOSHEATH
TRANSITION REGION
R = 13.8 R_e
LT = 11.6 HR
SELAT = 0.3°

Figure 13

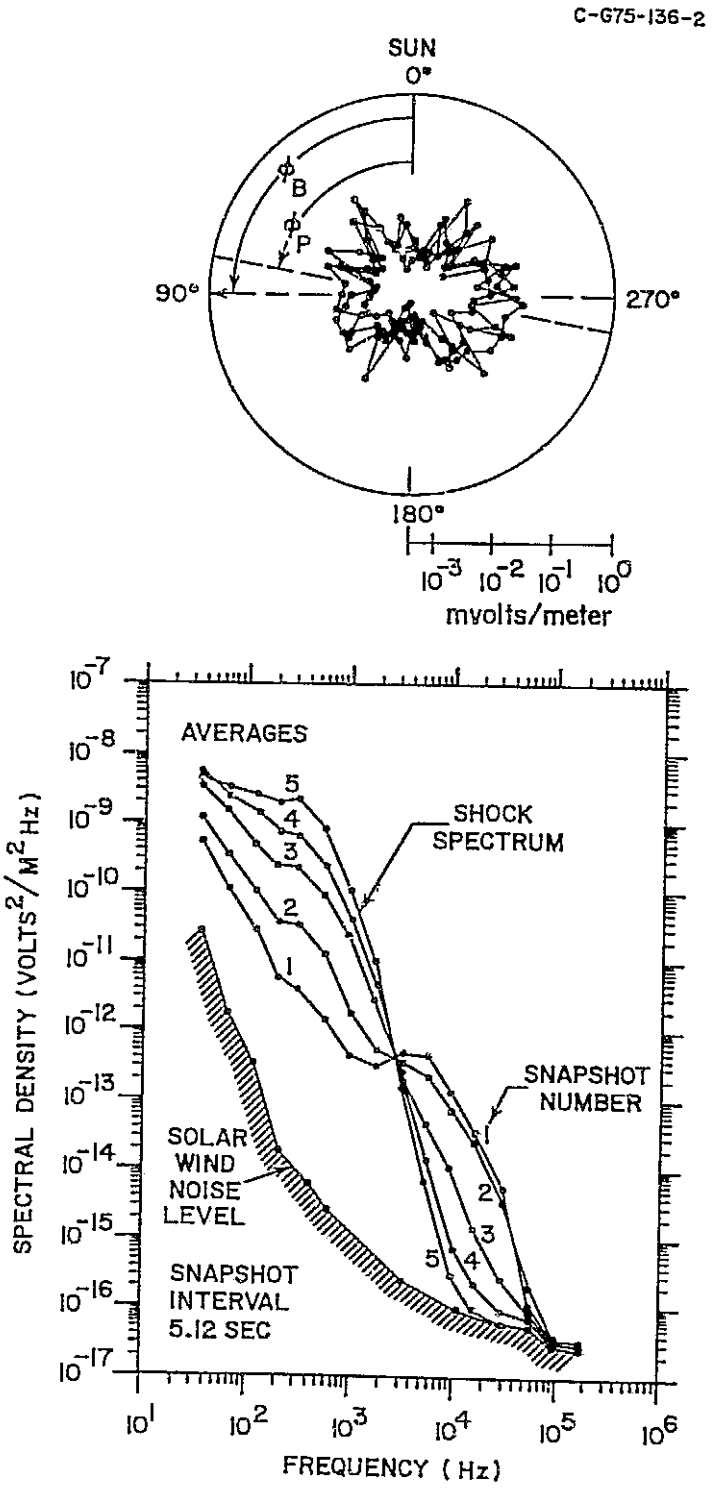
C-G75-136-2
SUN
0°
Φ_B
Φ_P
90°
270°
180°
10^{-3} 10^{-2} 10^{-1} 10^{0}
mvolts/meter
AVERAGES
SHOCK SPECTRUM
SNAPSHOT NUMBER
SOLAR WIND NOISE LEVEL
SNAPSHOT INTERVAL 5.12 SEC
SPECTRAL DENSITY (VOLTS^2/M^{2}Hz)
FREQUENCY (Hz)

Figure 14